Pitting corrosion inhibition of 304 stainless steel in NaCl solution by three newly synthesized carboxylic Schiff bases

M. Talebian[1], K. Raeissi[1,*], M. Atapour[1], B.M. Fernández-Pérez[2], A. Betancor-Abreu[2], I. Llorente[3], S. Fajardo[3], Z. Salarvand[4], S. Meghdadi[4], M. Amirnasr[4], R.M. Souto[2,5,*]

[1] *Department of Materials Engineering, Isfahan University of Technology, Isfahan 84156-83111, Iran*

[2] *Department of Chemistry, Universidad de La Laguna, Avda. Astrofísico Francisco Sánchez s/n, 38205 La Laguna (Tenerife), Canary Islands, Spain*

[3] *Department of Surface Engineering, Corrosion and Durability, National Centre for Metallurgical Research CENIM-CSIC, Madrid 28040, Spain*

[4] *Department of Chemistry, Isfahan University of Technology, Isfahan 84156-83111, Iran*

[5] *Institute of Material Science and Nanotechnology, Universidad de La Laguna, P.O. Box 456, 38200 La Laguna (Tenerife), Canary Islands, Spain*

*****Corresponding authors:

R.M. Souto, e-mail: rsouto@ull.es

K. Raeissi, e-mail: k_raeissi@cc.iut.ac.ir

Abstract

Three newly synthesized Schiff base derivatives, sodium (E)-4-(nitrobenzylideneamino)-benzoate (SNBB), sodium (E)-4-(benzylideneamino)-benzoate (SBB), and sodium (E)-4-(hydroxybenzylideneamino)-benzoate (SHBB) were investigated as pitting corrosion inhibitors for 304 stainless steel in neutral 0.1 M NaCl. Potentiodynamic polarization evidenced major shifts in pitting potential to more positive values with increasing inhibitor concentration. The scanning vibrating electrode technique (SVET) imaged metastable pitting in 0.1 M NaCl, but not in the presence of the inhibitor, indicating that it prevented pit nucleation. The inhibition performance was established under anodic polarization conditions, because only minute local anodic activity due to metastable pit formation could be observed when the steel was exposed to SNBB-containing solution, whereas the metal would undergo pit propagation at the same potential in the inhibitor-free solution. X-ray photoelectron spectroscopy (XPS) analysis evidenced chromium enrichment at weak points (pores) of the passive film at anodic polarization condition where sudden release of Fe cations is possible. In this way, the SNBB molecules will migrate to these sites to react with the Fe ions and form a chelate compound which will deposit finally at those sites and plug them, whereas no effect occurred at the open circuit potential (OCP).

Keywords: 304 stainless steel; Schiff bases; Corrosion inhibition; SVET; XPS; Pitting corrosion.

1. Introduction

Austenitic stainless steel (SS) is one of the most ubiquitous metallic materials due to its high corrosion resistance and strength, hygienic and aesthetic qualities, relative low cost, good formability, and weldability [1,2]. It is thus commonly found in a wide variety of applications such as chemical engineering, metal extraction industries, desalination and wastewater treatment plants, the oil and gas industry, transportation and aerospace industries, the food and beverage industry, and architecture and building engineering. It is well known that the high corrosion resistance of SS is related to the formation of a thin, adherent and protective passive film that forms rapidly on the surface [3,4]. Unfortunately, in the presence of certain aggressive ions like chlorides, the corrosion resistance of passive stainless steel is limited by local breakdown and pit nucleation [3]. In this form of corrosion, passivity breakdown occurs on small areas of the metal surface whereas the rest remains passive. Since nucleated pits occur on the microscopic scale and are frequently hidden by corrosion products, pitting corrosion is one of the most dangerous and widespread forms of localized corrosion in metals that often remains undetected producing catastrophic failures by perforation, or initiating stress corrosion cracks [4-6]. Breakdown is more likely to happen at susceptible sites in the passive film such as inclusions, second phase particles, flaws, and solute-segregated grain boundaries [7-9]. It is well known that pitting corrosion predominantly affects metals which are in the passive state, including various stainless steels, and the formation of corrosion pits is initiated by a pit nucleation step followed by two distinguishable propagation stages (namely, metastable growth and eventually stable growth). Pit initiation and transition to stability are the key factors controlling the overall pitting corrosion phenomenon [3,10,11].

An efficient and economical method of reducing metal dissolution in aggressive environments is the use of corrosion inhibitors [12]. A large number of organic molecules containing electronegative functional groups, such as π-electron systems (e.g., double or triple bonds, and aromatic rings) and/or heteroatoms (namely, N, S, P, O) have been proposed for the inhibition of general corrosion of metals [13-19]. However, the use of organic compounds as pitting corrosion inhibitors in neutral saline solutions remains still rather limited. It is well known that some organic compounds, especially surfactants, can act as inhibitors against the localized corrosion for stainless steels. Several mechanisms have been proposed to account for their inhibition properties, including competitive adsorption on the oxide film between inhibitors

and aggressive anions [20], interaction between inhibitor cations and the aggressive anions [21], and pore plugging in oxide films [22]. Guzmán and Lara [8] studied the inhibition behavior of 5-amino-1,3,4-thiadiazole-2-thiol for pitting corrosion of SS in 3.5% NaCl solution and reported that increasing the inhibitor concentration leads to more positive pitting potentials. Cardona et al. [23] evaluated the performance of an imidazole derivative as organic inhibitor for pitting corrosion of 316L SS in sulfuric acid solution at room temperature. They considered the compound as a good pitting corrosion inhibitor for SS in H_2SO_4 solution, assuming that the SO_4^{2-} ions induce the pitting corrosion process, although this assumption is at odds with other studies where the SO_4^{2-} ion is considered to inhibit pitting on metals [24]. Indeed, pitting corrosion of stainless steels occurs only in the presence of certain aggressive anions, mostly halides, whereas other non-aggressive anions such as ClO_4^-, SO_4^{2-}, NO_3^{2-}, and OH^- seem to inhibit the pitting corrosion of stainless steels [24,25]. In another study, Loto [26] investigated the performance of butan-1-ol (BtOH) on the pitting corrosion inhibition of 304 SS in sulfuric acid contaminated with NaCl, and he showed that BtOH enhanced the resistance of the steel to pitting corrosion. Alternately, inorganic-based compounds such as chromates and nitrates are also used as pitting corrosion inhibitors for SS in aggressive media [27,28]; however, the application of these inorganics, especially chromates and phosphates, is not recommended because of their biological toxicity [22,29]. Schiff bases and their complexes are non toxic and they find wide application in food industry, dye industry, analytical chemistry, catalysis, medicine, fungicidal, agrochemical and biological fields [30-32]. Schiff base derivatives with additional heteroatoms, such as N and O, and aryl groups, have also been used as corrosion inhibitors [14,17,33], but up to now, their application as pitting corrosion inhibitors has not been explored.

In this work, we report the synthesis of three novel carboxylic Schiff base derivatives and their application for the inhibition of the pitting corrosion of austenitic 304 SS. The design of these Schiff bases was aimed to improve their solubility in water and to enhance their coordination with the metal surface. These compounds containing the N and O heteroatoms, the imine group, and two benzene rings, were synthesized from the reaction of para-amino benzoic acid with selected aromatic aldehydes containing different functional groups in their para-position, with the aim of evaluating the effect of the functional group on inhibition performance of the Schiff base. The actual chemical structure of these inhibitors was confirmed using proton nuclear magnetic resonance (^{1}H NMR), and Fourier-transform infrared spectroscopy (FT-IR).

The inhibition efficiency of these compounds as pitting corrosion inhibitors for 304 SS in aqueous chloride solution was examined using a multiscale electrochemical approach consisting of surface-averaging potentiodynamic polarization measurements and the spatially-resolved scanning vibrating electrode technique (SVET). Post-mortem characterization of surface morphology and chemical composition was performed by scanning electron microscopy (SEM), and X-ray photoelectron spectroscopy (XPS).

2. Experimental

2.1. Synthesis and characterization of the new Schiff bases

Sodium (E)-4-(nitrobenzylideneamino)-benzoate (SNBB), sodium (E)-4-(benzylideneamino)-benzoate (SBB), and sodium (E)-4-(hydroxybenzylideneamino)-benzoate (SHBB), were synthesized using a two-step procedure. Firstly, the three Schiff base derivatives were synthesized by the condensation of 4-amino benzoic acid with a suitable benzaldehyde derivative. These compounds were subsequently converted to their sodium salt to obtain the target inhibitor molecules. According to a general procedure, (E)-4-(nitrobenzylidene-amino)-benzoic acid (NBB) was synthesized by drop wise addition of a solution of 4-aminobenzoic acid (5.5 mmol, 0.754 g) in 15 mL ethanol to a stirring solution of 4-nitrobenzaldehyde (5.0 mmol, 0.755 g) in 60 mL ethanol. The final solution was heated under reflux for 13 h producing a yellow precipitate. The reaction mixture was then allowed to cool while stirring, and poured into 70 mL of cold water. The solid product (NBB, 86% yield) was filtered off and washed with cold ethanol, and then recrystallized from a mixture of acetone and toluene. **(**E)-4-(benzylidene-amino)-benzoic acid (BB) and 4-[**(**E)-4-(hydroxy-benzylidene-amino)-benzoic acid (HBB) were synthesized by the same procedure, except that either benzaldehyde (5.0 mmol, 0.530 g) or 4-hydroxybenzaldehyde (5.0 mmol, 0.611 g) in 3 mL ethanol were employed instead of 4-nitrobenzaldehyde. In addition, 4 drops of acetic acid were added just before refluxing for 45 h. Finally, the solid product (BB, 60% yield) was filtered off after cooling the ethanolic solution. However, the mixture containing HBB was evaporated to dryness, and the remaining solid particles were washed with ethyl acetate (79% yield). Once purified, the resulting products were characterized by elemental chemical analysis, FT-IR and ^{1}H NMR, before undertaking the second step of the synthetic route.

The deprotonation constant (pK_a) of NBB and the stability constant of Fe^{2+}-SNNB complexes were determined pH metrically by the Irving-Rossotti method [34] at room temperature. The following three solutions were prepared in total volume of 25 mL and titrated with NaOH standard solution 0.1 M at constant ionic strength (2×10^{-2} M $NaClO_4$), namely, (Solution 1): 2.5 mL $HClO_4$ (2×10^{-2} M) +2.5 mL $NaClO_4$ (2×10^{-2} M), (Solution 2): Solution 1 + 5 mL NBB (1×10^{-2} M), and (Solution 3): Solution 2 + 1 mL Fe^{2+} ion (1×10^{-2} M).

Solutions containing the sodium salt of the Schiff base derivatives were prepared taking in account the corresponding pK_a value for each species. A specific mole amount of each Schiff base was added to water and titrated with equal moles of sodium hydroxide. In brief, for the preparation of 10 mM solution of SNBB, 0.675 g (2.5 mmol) NBB was suspended in 50 mL water, then titrated with 50 mL sodium hydroxide solution (0.05 M) to attain pH = 7.0 (as the determined pK_a value was 6.8), and the volume was made up to 250 mL by adding deionized water. The same procedure was employed for the preparation of 10 mM solution of SBB and SHBB, by using 0.563 g of BB and 0.603 g of HBB instead of NBB.

2.2. Sample preparation and test electrolyte solution

AISI 304 austenitic SS, with chemical composition (wt.%): Cr 18.529, Ni 8.545, Mn 1.309, Si 0.331, Cu 0.303, C 0.063, P 0.036, S 0.025 and Fe balance, was used in this study. The metal was analyzed using ARUN METALSCAN 2500 Optical Emission Spectrometer. Two types of samples were prepared for the electrochemical tests. Conventional electrochemical testing was performed using disk shape specimens cut to approximately 1 cm^2 area. The electrical connection was carried out by welding a Cu wire to the back part of the sample, before being cold mounted in epoxy resin. Consequently, only one face was exposed to the electrolyte. For the SVET tests, 304 SS sheets of 1 mm thickness were cut into 60 mm × 2 mm strips, and then embedded vertically in an insulating resin. To facilitate the electrical connections required for the application of a potentiostatic polarization, the metal strips were allowed to protrude at the rear part of the mount. Prior to each measurement, the samples were ground using a sequence of silicon carbide emery papers ranging from 240 to 2000 grit size, subsequently rinsed using Millipore deionized water and acetone, and finally dried under warm air flow. It should be noted that the surface laboratory condition applied in this study is different from typical industrial conditions, but it can provide a good starting point to the industrial use of these inhibitors.

The aqueous test solution (0.1 M NaCl) was prepared by dissolving the reagent-grade chemical in deionized water (Milli-Q® ultrapure water quality, resistivity 18.2 MΩ cm). Different concentrations of the inhibitors, ranging from 1 to 10 mM, were added to the test solution.

2.3. Electrochemical measurements

Conventional electrochemical measurements were performed using an AMETEK potentiostat/galvanostat model PARSTAT 2263 controlled by *PowerSuite* software. A three-electrode configuration was used with the 304 SS sample, a platinum ring, and the saturated calomel electrode (SCE, E^0 = +0.240 V_{SHE}) acting as the working (WE), counter (CE) and reference (RE) electrodes, respectively. The fresh surface of the WE was exposed to 250 mL of 0.1 M NaCl solution, either in the presence or the absence of the inhibitors, under static aerated conditions at the laboratory temperature (25 ºC). Prior to potentiostatic polarization of the metal sample in the actual electrochemical measurement, the WE was immersed in the test electrolyte for 1 h until a stationary open circuit potential (OCP) was attained. Potentiodynamic polarization measurements were performed with the scan rate of 0.5 mV s^{-1}. The potential scan was initiated from -0.25 V with respect to the OCP, by sweeping the potential in the positive direction until the current density exceeded 1 mA cm^{-2}, which was then reversed to the negative direction, and repassivation was achieved with a crossing point at the repassivation potential. The measurements were performed in triplicate, and the average values are reported. The pitting potential (E_{pit}) was determined from the anodic branch of the potentiodynamic polarization curves as the potential value where a sudden increase in the current density occurred [11]. Alternately, potentiostatic current transients were recorded on freshly prepared samples after OCP stabilization for 1 h by applying a potential step from E_{corr} to +0.40 V_{SCE} for 600 s.

Scanning microelectrochemical characterization was performed using a SVET device manufactured by Applicable Electronics Inc. (Forestdale, MA, USA), which was controlled by dedicated software. The sensing probes were 10 µm Pt-Ir (80%-20%) wires insulated by paralene C® and arced at the tip to expose the metal. The wires were platinized under constant current operation to produce a spherical platinum black deposit of 10-20 µm diameter. A video camera coupled with an optical microscope was used to establish the distance between probe and sample, as well as to follow the movement of the electrode tip vibrating over the sample during

measurements. The mounted samples were surrounded laterally by Sellotape to create a small container on the sample under study, thus the electrolyte covered the sample by a ca. 8 mm liquid column. The electrochemical cell for SVET operation was completed by using the spherical platinized probe and a Pt wire as reference electrode. A reference measurement with the microelectrode away from the active area was subtracted from the values measured during the scan. The measurements were made with the probe vibrating in a plane perpendicular to the sample (vibration amplitude, 10 µm). The mean distance between the microelectrode and the sample surface was 50 µm. For the experiments under potentiostatic polarization conditions, an Ag/AgCl/(3 M) KCl reference electrode and a platinum ring counter electrode were added to the small electrochemical cell, whereas the exposed metal sample was connected as the WE. For the sake of consistency and ease of comparison, all the potential values mentioned in this work are expressed with regards to the SCE as reference. Electrochemical control was carried out using a potentiostat model 283 from EG&G Instruments. The SVET measurements were carried out at ambient temperature (nominally 25 °C) in an aqueous 0.1 M NaCl solution.

2.4. Surface characterization

The effects of SNBB on the morphology and the surface composition of 304 SS samples were investigated both prior and after the application of the potentiostatic polarization described in Section 2.3. Surface characterization of the samples retrieved from the conditioning test solution was performed after being ultrasonically cleaned in ethanol. SEM was performed using a model JSM-5310 microscope from JEOL.

XPS was performed using a Fisons MT500 spectrometer equipped with a hemispherical electron analyzer (CLAM2) and a non-monochromatic Mg Kα X-Ray source (E = 1253.6 eV) operated at 300 W. The samples were fixed on small flat discs supported on an *XYZ* manipulator placed inside the analysis chamber. The residual pressure in this ion-pumped analysis chamber was maintained below 10^{-8} torr during data acquisition. The spectra were collected under constant pass energy of 20 eV, which is typical of high-resolution conditions. Although sample charging was observed, it was possible to determine accurate binding energies by referencing to the adventitious C 1s peak at 285.0 eV. Three different emission angles (namely, 5, 20 and 45 degrees) were used with the aim of investigating the chemical composition of the outermost regions of the surface layer. This method, known as angle resolved XPS (ARXPS), allows for the

non-destructive analysis of ultra-thin films without sputtering by varying the emission angle at which electrons are emitted from the surface.

3. Results and discussion

3.1. Chemical structure of the new Schiff base derivatives

The chemical structures of the synthesized Schiff base derivatives were characterized using elemental analysis, FT-IR and ^{1}H NMR characterizations. As an example, the element analysis for the NBB molecule is given in Table 1. The results confirm the molecular formula to be $C_{14}H_{10}N_2O_4$ (MW = 270.24 g mol^{-1}). The FT-IR spectrum of this molecule (in KBr pellet) recorded from 400 to 4000 cm^{-1} is shown in Figure 1. Bands associated with the OH, C=O and C=N functional groups were observed at υ_{max} (cm^{-1}): 3500-2500 (OH), 1683 (C=O), 1601 (C=N). Therefore, the recorded FT-IR spectrum confirmed the presence in the NBB molecule of the expected functional groups [35-39]. The ^{1}H NMR spectrum (500 MHz, chemical shift (δ) in ppm) of NBB in DMSO-d_6 (CD_3SOCD_3) in Figure 2, displayed three bands, namely δ = 7.38-8.38 ppm (4d, 8H, Ar-H); δ = 8.82 ppm (s, 1H, CH=N); and δ = 12.77 ppm (s, 1H, Acid-H). These results confirm the expected type and also the proton distribution in NBB molecule. Similar results were obtained for the BB and HBB molecules confirming their corresponding molecular formula. Table 2 summarizes the chemical structures and molecular weights of the three Schiff base derivatives synthesized in this work.

3.2. Potentiometric characterization of the new Schiff base derivatives

The pH-metric measurement method can be used to determine the stability constant of complexes whenever the formation of the complexes is considered to be due to the displacement of a proton from the ligand. The pK_a of NBB and then the stability constants (logK_1 and logK_2) of Fe^{2+}-SNNB complexes were determined pH-metrically. The ligand solution and the mixture of ligand and Fe^{2+} ion solutions were acidified with $HClO_4$ and the ionic strength was kept constant with $NaClO_4$ solution. The titration of the three solutions described in Section 2.1 was carried out at room temperature. The measured titration curves (pH vs. added volume of NaOH) are shown in Figure 3.

The average number of protons associated with NBB, $\bar{n}_A$, was calculated at different pH values using Irving-Rossotti equation [34]:

$$\bar{n}_A = \gamma - \left[\frac{\left(C^0 + N\right)\left(V_2 - V_1\right)}{\left(V^0 + V_1\right)T_1^0} \right] \quad (1)$$

where γ is the number of dissociable protons (here $\gamma = 1$), N is the concentration of NaOH, V_1 and V_2 are the volume of NaOH added to reach the same pH in titration of Solutions 1 and 2, C^0 and T^0 are the concentration of sodium perchlorate and the ligand, respectively, and V^0 is the initial volume of the reaction mixture (25 mL). The titration curve for the mixture $HClO_4$ + SNBB shows only one inflection point, a feature indicating that there is only one acid group, and the proton dissociation constants for NBB (referred as *HL*) were determined using the following equation [40]:

$$HL \rightleftharpoons H^+ + L^- \quad (2)$$

$$K' = \frac{[H^+][L^-]}{[HL]} \quad (3)$$

The value of p*K* was determined using the half-integrated method by plotting $\bar{n}_A$ vs. pH as it is shown in Figure 4, and it was found to be 6.8.

In a similar manner, the metal ligand stability constants were determined pH-metrically as well. The related titration curve showed in Figure 3 and well separated from that for SNBB, thus confirming that the formation of the complex happened with the release of one proton [41]. The formation curve of the complex was obtained from the $\bar{n}$-p*L* plot, where $\bar{n}$ is the average number of ligand attached per metal ion and p*L* is the free ligand exponent. The experimental $\bar{n}$ values were determined using the following equation:

$$\bar{n} = \left[\frac{\left(C^0 + N\right)\left(V_3 - V_2\right)}{\left(V^0 + V_2\right)T_m^0} \right] \quad (4)$$

where N, C^0, V^0 and V_2 have the same definitions as for Eq. (1), whereas V_3 is the volume of NaOH in the metal titration to attain the given pH, and T_m^0 the initial concentration of the metal ion. It is observed that at pH = 2, free metal ions were present in 99% amount, and this percentage decreased gradually with increasing the pH of the solution until they attained an almost zero value at higher pH. This fact suggests that, with increasing pH of the solution, the

metal ions are distributed in ML species for all metal-ligand complex systems in the pH range. The reaction mechanism of complex equilibria could be as it follows:

$$HL \rightleftharpoons H^{+} + L^{-}, \quad (5)$$

$$M^{2+} + L^{-} \rightleftharpoons ML^{+}, \quad (6)$$

$$ML^{+} + L^{-} \rightleftharpoons ML\ . \quad (7)$$

The stability constants of the investated system have been evaluated by using the half-integral method [34,42]. Although it was found that logK_1 is bigger than logK_2, respectively 6.3125 and 5.2610, the difference is not sufficient to prevent the simultaneous formation of the Fe^{2+}-SNBB complex.

3.3. Potentiodynamic polarization measurements

At first, the polarization behavior of 304 SS was examined in the presence of various concentrations of SNBB, and next, the effect of the functional group on the inhibition performance of the Schiff base was evaluated. For the sake of comparison and reproducibility, prior to applying potential in each electrochemical test, the WE was left unpolarized for 1 h in the corresponding test solution. Figure 5 shows the evolution of the OCP as a function of time for the 304 SS surface immersed in 0.1 M NaCl in the inhibitor-free solution and in the presence of different concentrations of SNBB (i.e., 1, 5, and 10 mM). It is observed that the OCP remained almost constant (around -0.16 V_{SCE}) after 1 h of immersion in the absence of the inhibitor, while in the presence of inhibitor the variation of potential with respect to time ($\Delta E/\Delta t$) was less than 10^{-5} V s^{-1} during the last 100 s, which is indicative of the steady state condition.

Typical cyclic potentiodynamic polarization plots of 304 SS immersed in 0.1 M NaCl with various concentrations of SNBB are depicted in Figure 6. The establishment of well-defined passive regions at potentials more positive than the corresponding OCP is readily observable from the potentiodynamic polarization curves. The breakdown of the passive regime was monitored as an abrupt increase in the current density at sufficiently positive polarizations. The sharp increase of the current density values with the shift of potential was indicative of the occurrence of a stable pitting regime. The values of the pitting potential (E_{pit}) were higher in the presence of SNBB and tended to increase with the concentration of inhibitor in the test solution.

The observed positive hysteresis loop confirms the occurrence of pitting corrosion. The potential at which the reverse scan crosses the forward one is defined as the repassivation potential (E_{rp}). In addition to E_{pit} and E_{rp}, values of other relevant electrochemical parameters were extracted from the cyclic potentiodynamic polarization curves, namely the corrosion potential (E_{corr}), the corrosion current density (j_{corr}), the passivation current density (j_{pass}), and the width of the stable passive region (determined as E_{pit} - E_{corr}). These parameters are listed in Table 3 for SNBB as well as for SHBB and SBB (although they will be discussed later in this Section). They are given as the average values from three separate measurements along with their corresponding standard deviations. It is noteworthy that the addition of SNBB to the test solution produced no observable significant effect on the shape of the cyclic potentiodynamic polarization plots for potential values below the pitting potential of 304 SS in 0.1 M NaCl solution. That is, very small variations are observed among the values of the electrochemical parameters related to either general corrosion (i.e., E_{corr} and j_{corr}) or the establishment of passivity (e.g., the passive current density, j_{pass}) regardless of being measured in the absence or in the presence of this Schiff base. However, the addition of SNBB to the test solution resulted in an enlarged passive region for the steel, owing to the big shift in E_{pit} values to more positive potentials, with a maximum shift of 230 mV when the test solution contained 10 mM SNBB. It is well known that metals and alloys with wider stable passive regions and higher values of E_{pit} are more resistant to pit nucleation [43]. Therefore, the results given in Table 3 demonstrate the ability of SNBB to enhance the pitting corrosion resistance of 304 SS in neutral NaCl solution. The effect of SNBB concentration on the shift of the pitting potential of 304 SS is more easily observed from an inspection of Figure 7. The increase in E_{pit} with the concentration of inhibitor is readily observable, a feature that evidences the efficient inhibition performance of SNBB against pit nucleation on 304 SS in neutral chloride solution. However, it is clear from Figure 6 that the slope of the curves after pitting occurrence remained unchanged by varying the inhibitor concentration except for the addition of 10 mM SNBB. This means that the inhibitor did not affect pit growth for the smaller concentrations [22]. Therefore, the enhanced protection provided by SNBB to 304 SS must be related to pit nucleation. According to Table 3, E_{rp} values were not modified by the presence of SNBB in the test solution, which means no effect on pit repassivation. Based on the extent of the hysteresis loop (cf. Figure 6), it can be concluded that, if a stable pit forms, its propagation would not be prevented in the presence of SNBB. In general,

it is almost impossible to prevent pitting growth due to the autocatalytic nature (self-stimulating and self-propagating process) of the pit continuing activity. This is supported by an excess of positive charge inside the pits which pulls chloride ions and promotes water hydrolysis originating a significant pH drop inside the pits [11,22].

Next, the effect of the functional group on the inhibition performance of the Schiff bases was investigated by assessing the electrochemical behavior of two other similar molecules with different functional groups at the para- position of the aromatic aldehyde (SHBB and SBB). For the sake of comparison, a 10 mM concentration of the different inhibitors was added to a 0.1 M NaCl solution in separate experiments. The potentiodynamic polarization curves of 304 SS steel in these solutions are shown in Figure 8. The values of the electrochemical parameters extracted from these plots are summarized in Table 3. It was observed that rather small variations in these electrochemical parameters resulted from the change in the functional group attached to the terminal aromatic ring of the inhibitor molecule, thus supporting the fact that the nature of the functional groups attached to the aromatic aldehydes does not greatly modify the pitting corrosion inhibition mechanism of 304 SS in neutral chloride solution. Nevertheless, a more positive E_{pit} value was determined in the case of SNBB. Therefore, SNBB was selected for further characterization so as to investigate the interaction of the SNBB molecule with the surface of this steel.

3.4. Potentiostatic polarization and SEM characterization

Chronoamperometric curves resulting from the application of a positive potential to the 304 SS samples under potentiostatic polarization at +0.40 V_{SCE} during immersion in 0.1 M NaCl solution with and without 10 mM SNBB were performed to investigate the susceptibility to passive layer breakdown of the oxide films formed on the alloy. This potential was selected as an intermediate compromise between the E_{pit} values determined for the steel in the inhibitor-free solution and in the presence of the inhibitor. That is, chloride ions would promote the breakdown of the oxide layer, pit nucleation and stable growth in the absence of an efficient pitting corrosion inhibitor, whereas passive layer growth would be the only relevant electrochemical contribution to current flow in the electrochemical cell in the case of efficient inhibition. Figure 7 shows typical current density versus time curves of 304 SS samples under potentiostatic polarization at +0.40 V_{SCE} during immersion in 0.1 M NaCl solution with and without the

addition of 10 mM SNBB. Current density values initially decreased with the elapse of time, eventually leading to the establishment of an apparent stationary passive current density value both in the presence and in the absence of SNBB. However, after about 120 s the current density recorded for the sample exposed to the inhibitor-free test solution increased due to metal dissolution resulting from the nucleation and growth of corrosion pits. By contrast, the current density transient recorded in the presence of SNBB stayed constant during the remaining time of the experiment (i.e., up to 600 s), providing solid evidence of the steel resistance against pit formation. It may be of interest for future studies to extend the testing time beyond 600 s.

Chronoamperometric data were supported by SEM characterization of the 304 SS samples after potentiostatic polarization at +0.40 V_{SCE} for 600 s, both in the absence and in the presence of 10 mM SNBB in 0.1 M NaCl solution. Typical micrographs from each case are displayed in Figure 10. Figure 10a shows that the surface of the SS was extensively attacked, with several pits randomly distributed across the surface. By contrast, no localized attack was observed after polarization in the presence of 10 mM SNBB despite the application of an anodic potentiostatic pulse to the metal for 600 s (see Figure 10b). These results support the ability of SNBB to inhibit pitting corrosion for stainless steel in neutral chloride solution.

3.5. Scanning vibrating electrode technique

Although the conventional electrochemical tests described in the previous sections allowed the superior performance of SNBB to prevent the onset of pitting corrosion of 304 SS in neutral NaCl solution, the recorded data only provide an average characterization of the material. In order to further investigate the pitting inhibition performance of SNBB in aqueous chloride solution from spatially-resolved measurements in the micrometric scale, this system was also investigated using SVET. SVET is based upon the measurement of potential gradients in the electrolyte phase surrounding an electrochemically-active surface. A vibrating pseudo-reference electrode was employed to scan the metal surface. Therefore, unlike conventional electrochemical tests which give only an average response of the reactivity of the whole electrode surface, SVET can synthesize data concerning the eventual establishment of local nanometric and/or micrometric cells on an active surface depending on the sample to probe height [44-47].

Figure 11 shows SVET images recorded over 304 SS sheets after 60 min immersion in 0.1 M NaCl under open circuit using SVET. These graphs only display the background noise signals related to self-passivation of the metal surface in the electrolyte when the samples were kept unbiased in the test solutions regardless of whether the inhibitor was present or not. That is, no effect of SNBB on the local reactivity of 304 stainless steel sheets towards localized passivity breakdown at the micrometer scale could be distinguished by recording ionic current density maps over SS samples left at their corresponding OCP. Such featureless behavior is in agreement with previous characterizations of stainless steel samples subjected to diverse surface treatments for enhanced corrosion protection when they were imaged using SVET during immersion in aqueous chloride solution at their OCP [48,49].

Therefore, the application of an anodic polarization to the metal samples for electrochemical activation of the immersed surfaces was considered next. Firstly, a potentiostatic polarization step at +0.40 V_{SCE} was applied to the 304 SS samples immersed in the chloride solution both in the absence and the presence of SNBB. The resulting ionic current density distributions are displayed in Figure 12 for each solution. In the inhibitor-free solution, the SVET maps showed distributions of a highly localized and intense anodic electrochemical activity occurring on the upper side of the image, therefore occurring at a certain specific area on the exposed surface of the stainless steel (cf. Figure 12a). This high ionic current density arose from the active dissolution of the steel that released metal cations into the electrolyte solution from a propagating corrosion pit. An additional relevant feature is the observation of a rather extended cathodic area on the steel's surface proximal to the corrosion pit (evidenced by the blue-colored region). Although the use of a potentiostat for the application of an anodic potential to the steel sample would cause the corresponding cathodic processes to occur at the auxiliary electrode, effectively remote from the corroding sample, some cathodic activity would still be sustained on the steel surface immediately adjacent to the fast propagating corrosion pit. Indeed, the total ionic currents related to the cathodic half-cell reaction for oxygen reduction on the steel surface only amounted to approximately one-tenth of those related to the anodic metal dissolution. Despite such an imbalance, the local cathodic activity adjacent to the corroding pit would account for the alkalization of the electrolyte volume adjacent to the metal surface, thus favoring the precipitation of iron oxy-hydroxides. The development of a corrosion pit and the precipitation of corrosion products in the proximity of the corroding pit was further confirmed by

the optical image recorded using the in-built video camera in the SVET set-up (also shown in Figure 12a). Whereas most of the steel surface remained almost unchanged, the onset of metal dissolution and corrosion products precipitation mostly occurred around the nucleated corrosion pit.

A very different SVET image was obtained for the 304 SS sample polarized in the test solution containing SNBB compared to the results obtained at its OCP. In this case, the SVET map displayed an ionic current distribution that was almost completely featureless except for the occurrence of four very small anodic peaks slightly above the background noise signal. Indeed, it should be noted that the ionic current density range of Figure 12b is 25 times smaller than the corresponding one exhibited in Figure 12a, and almost comparable to those shown in Figure 11. In addition, it should also be observed that these four anodic current peaks were almost one-dimensional in shape, since they developed along the current recording scan line, but could not be found when the vibrating probe passed again above the same sites on the surface while recording the following scan line. Since the time taken to complete a scan line of the exposed surface is much longer than the average lifetime of a metastable pit, these anodic current density peaks disappeared in the next scan line. Therefore, these anodic ionic current density peaks were of a very short duration, and could be attributed to the initiation and subsequent repassivation of metastable pits. These results are in agreement with the observations derived from potentiodynamic polarization curves that showed that the anodic polarization at +0.40 V_{SCE} lied within the passive region of 304 SS in the presence of SNBB (cf. Figure 6 and Table 3). That is, the potential applied to the sample is more negative than E_{pit} of stainless steel in 0.1 M NaCl containing 10 mM SNBB. The visual appearance of the stainless steel surfaces at the end of SVET test in Figure 12 confirms the high performance of SNBB on inhibition of pitting corrosion of 304 SS in neutral chloride-containing solutions, where an intact metal surface was imaged using the video camera despite the anodic polarization applied to the sample.

The detection of metastable pit nucleation and repassivation using the SVET occurred for the steel sample left unpolarized during immersion in 0.1 M NaCl that was shown in Figure 11a. In fact, various short-lived anodic peaks could also be observed in this SVET map, indicating that minute breakdown events related to metastable pitting occurred on 304 SS immersed in neutral aerated NaCl solution even under open circuit conditions. Conversely, no similar events could be observed when the SS sample was immersed in the test solution containing SNBB (cf.

Figure 11b). The in situ imaging of metastable pitting events on 304 SS in aqueous chloride solution under OCP conditions using SVET is a very noteworthy observation from this work, a feature only described thus far using high resolution scanning electrochemical microscopy (SECM) in the generation-collection amperometric operation mode, and when this material was exposed to a more aggressive environment of 0.1 M HCl [49]. In contrast, the associated cathodic process could not be detected this time because of the combined effect of the larger tip-sample distance required for the operation of the vibrating probe in SVET compared to the stagnant Pt microdisk tip employed in SECM, that implies a wider spot size for SVET, and the very minute ionic currents involved in the process this time. That is, since the anode to cathode distance is smaller than the height of the vibrating probe scanning over the sample, the current flux lines arising from a larger cathodic area do not cross the plane of scan [50]. Consequently, the associated cathodic process could not be resolved above the background noise signal. On the other hand, the observation of resolved metastable pitting events at the OCP in 0.1 M NaCl solution and their absence in the solution containing SNBB is an indication that the corrosion inhibition action of SNBB for 304 SS operates by preventing passive layer breakdown even at the initial pit nucleation stage. Although these are short-lived breakdown events, selective iron dissolution occurs at these sites [51], leading to local Cr enrichment in the corresponding sites. Therefore, SNBB has been shown to operate already under OCP conditions, although the very low breakdown frequency occurring in a potential range well below the corresponding E_{pit} value neither allow such minute localized breakdowns to be resolved at the level of the recorded potentiodynamic polarization curves (see Section 3.3) nor to produce an observable chemical composition modification as observed by XPS (cf. XPS analysis of Sample code III in Section 3.6 below). Therefore, the power of combining conventional and scanning microelectrochemical techniques for the characterization of this metal-inhibitor system has proven to provide valuable complementary information that was not accessible using exclusively one kind of experimental approach.

Finally, with a further increase of the applied anodic potential up to +0.50 V_{SCE}, an intense and localized corrosion attack happened on the 304 stainless steel strip even in the presence of SNBB (Figure 13) due to the establishment of a stable pitting corrosion regime. Although most of the metal dissolution originated from the corrosion pit developed on the upper right part of the map, the earlier stages of another nucleated pit can be observed in a more central

location. In this case, no cathodic sites could be observed on the corroding surface due to the higher driving force to produce the cathodic reactions at the auxiliary electrode. As a result, less alkalization of the electrolyte volume could occur during the rather short duration of the SVET measurements, resulting in the visualization of the corrosion pit without precipitation of corrosion products in its neighborhood according to the optical micrograph shown in Figure 13. Although some precipitates of corrosion products were still visible in the micrograph, they were mainly randomly distributed over the exposed steel sample in this case.

It must be noticed that, if another type of localized corrosion (i.e., crevice corrosion) had occurred in the specimen, the SVET would be able to detect it, as well as to show how SNBB could greatly hinder it.

3.6. XPS analysis

The inhibitive action of SNBB to prevent the initiation of pitting corrosion on 304 SS in neutral 0.1 M NaCl solution was further investigated using XPS. This provided information on the chemical composition of the inhibited metal surface compared to that of the uninhibited metal. Four different conditionings were applied to the steel samples for XPS analysis as described in Table 4. They were selected so as to replicate the various conditions that could be experienced by a steel surface in the different situations considered in this work. Thus, chemical information was gathered on the surface of pristine metal (sample I), on the surface film spontaneously formed on the metal under OCP conditions both in the absence (sample II) and in the presence (sample III) of the inhibitor in the test solution, and on some local yellow points detected on the sample surface subjected to anodic polarization (+0.45 V_{SCE}) in the presence of SNBB (sample IV). In addition, the XPS spectra were collected by analyzing, for each given spot site at different emission angles (namely, 5, 20, and 45 degrees), the corresponding spectra to obtain information on the in-depth distribution of the chemical elements and their oxidation states. The total sampling depth of the XPS measurement is given by the following equation: $d = 3\lambda \cos \theta$; where λ is the attenuation length of electrons in the polymer film and θ the angle between the analyzer and the surface normal direction (i.e. emission angle) [52,53]. XPS measurements were performed at three different locations on each sample for the sake of reproducibility.

As a representative illustration, Figure 14 shows the high-resolution spectra of Fe $2p_{3/2}$, Cr $2p_{3/2}$, Ni $2p_{3/2}$, N 1s, C 1s, and O 1s. All high-resolution spectra shown in Figure 14 were recorded at an emission angle of 5 degrees in the case of sample II, with the exception of that corresponding to N 1s that was recorded at the same emission angle but in sample IV as this was the only sample that showed a clear signal for N 1s. The high-resolution Fe $2p_{3/2}$ signal in Figure 14a was deconvoluted into four peaks corresponding to the oxidation states 0, +2 and +3 of iron, the latter presenting two separable peaks for Fe_2O_3 and FeOOH, respectively. In the case of chromium, only oxidation states 0 and +3 were observed, accounting for the three deconvoluted peaks shown in Figure 14b. Analogously, two oxidation states were also found for Ni $2p_{3/2}$ in Figure 14c. As mentioned before, sample IV was the only one showing an unambiguous signal for N 1s, thus demonstrating the occurrence of a specific metal-inhibitor interaction in this case. Finally, the C 1s spectrum exhibited three peaks corresponding to aliphatic and to oxygenated carbon bonds, whereas the O 1s spectrum was not sufficiently resolved as to allow the unambiguous separation of the contributions from Fe, Cr and Ni oxy-hydroxides.

The influence of the inhibitor on the composition of the surface oxide layers, developed on stainless steel, could be better ascertained from an inspection of Figure 15. In this case, the atomic concentrations of the oxide components of Fe, Cr and Ni were plotted as a function of the emission angle for the four samples under investigation. It is observed that the amount of oxidized Fe showed the highest values for samples I and II, but decreased in the presence of the inhibitor. Furthermore, a significant decrease in Fe content was observed for the previously polarized sample (i.e., sample IV). In the case of Cr, the oxide percentage showed the highest values for samples II and IV, which exhibited very similar behavior. It is interesting to note the differences observed between the sample in the presence of the inhibitor and in the absence of polarization with the one that was previously polarized. For Ni, samples I and II showed a similar amount of Ni-oxides in the passive layer, but this amount decreased in the presence of the inhibitor, and it was not detected after polarization (sample IV).

In order to evaluate changes in the oxide layer composition, the cationic fractions of Cr and Fe are plotted in Figure 16 as a function of the emission angle. The cationic fraction was calculated as the ratio between the oxide components of a given element divided by the sum of all the metallic oxide components detected in the passive film. For instance, the cationic fraction of Cr was Cr(ox)/[Cr(ox)+Fe(ox)+Ni(ox)]. It is observed that for the reference sample (i.e.,

sample I) the oxide layer was mainly composed of oxidized species of Fe; whereas Cr oxides showed the greatest contribution after anodic polarization, becoming the main component of the passive layer. For samples II and III, Figure 16 shows that at an emission angle of 45 degrees (i.e. the outermost part of the surface layer), the majority of the passive film (about 65%) was composed of oxidized species of Fe while Cr-oxides contributed about a 30%. Note that passivity of stainless steels is usually attributed to the presence of oxidized species of Cr in the surface layer. Therefore, the efficient pitting corrosion inhibition provided by the SNBB to anodically polarized 304 SS arose from the chemical interaction of this organic compound with an enriched Cr environment. According to these results, it is proposed here that the pitting corrosion inhibition provided by SNBB to the anodically polarized 304 SS is associated with the occurrence of an enriched Cr film during anodic polarization, and this organic molecule would preferentially interact with this Cr-rich layer. The measurable signal for N in sample IV provides evidence for the occurrence of a specific metal-inhibitor interaction (i.e., chemical adsorption).

3.7. Mechanism of pitting corrosion inhibition

Since the breakdown of passive film is promoted by adsorption of aggressive anions such as chloride (especially at high potentials), inhibition of pit nucleation can be commonly achieved by reducing the extent of aggressive anion adsorption on the passive film surface through competitive adsorption of other chemical species. The relationship between the pit nucleation potential (E_{pit}) and the concentration of the inhibitor (C_{inh}) is given by [22]:

$$E_{pit} = a + b\log\left(\frac{C_A}{C_{inh}}\right) \quad (8)$$

where C_A is the concentration of aggressive anion (chloride ions) which is constant in this study. As observed from Figure 17, there is not a linear relation between E_{pit} and $\log(C_{inh}^{-1})$. Thus, the competitive adsorption of the SNBB molecules with chloride ions and the subsequent removal of chloride ions from the electrode surface cannot be considered to be the dominant mechanism here [54].

An alternate inhibition mechanism for pit nucleation is pore plugging as proposed by Evans [55]. According to this theory, the inhibitor repairs the weak points (pores) created in the passive film. The breakdown starts at the pores in the passive film of SS giving rise to strong local release of Fe cations. Since the SNBB molecule is a strong chelator and can form stable

chelates with the Fe(II) ions [33], the SNBB molecules may migrate to these sites to react with the Fe ions and form chelates (with stability constants $\log K_1 = 6.3125$ and $\log K_2 = 5.2610$) which will deposit finally at these sites and eventually plug them [22,52].

It should be noticed that the Evans' theory does not provide a complete explanation of the action of inhibitor. In some instances, it is suggested that the inhibitive effect is exerted through a relatively labile adsorption on the oxide surface rather than irreversible incorporation into the pores of oxide film [56]. On the other hand, for the organic molecules, it is believed that they just screen the pores presented in the passive film after adsorption, in preference to aggressive ions [54].

4. Conclusions

In this study, the pitting corrosion susceptibility of the austenitic 304 stainless steel in neutral chloride-containing solution and its inhibition using Schiff base compounds was characterized using a powerful combination of multiscale electrochemical and surface analytical techniques. The following findings can be summarized:

- Novel Schiff base compounds have been synthesized to operate as pitting corrosion inhibitors for austenitic 304 stainless steel in neutral chloride-containing solution, and their chemical structures were characterized using elemental analysis, FT-IR and ^{1}H NMR.
- The use of conventional electrochemical characterization methods provided solid evidence that the inhibitive action of these molecules produced big shifts of the pitting potential of 304 SS in 0.1 M NaCl towards more positive values, thus leading to the establishment of a more extensive passive regime for this material.
- Changes in group functionality at the terminal aromatic ring of the inhibitor did not produce major changes in the inhibition efficiency of the corresponding Schiff base compound, although the best inhibition performance was provided by SNBB in terms of both wider potential region of stable passive regime, and more positive pitting potentials.
- The enhanced pitting resistance of stainless steel 304 obtained by the presence of SNBB could be attributed to pore plugging of the passive film. In the inhibitor-free solution, the SVET maps show how electrochemical activity develops on the surface of the material resulting from localized breakdown of the passive layer, as either metastable or stable pitting depending on the electrical state of the steel sample. However, in the presence of SNBB, the

SVET images reveal only the limited local anodic activity at some points due to the formation of metastable pits at anodic polarizations above the E_{pit} value of the steel in the inhibitor-free solution. Moreover, SNBB prevents metastable pitting, which indicates that the corrosion inhibition action of this inhibitor prevents passive layer breakdown at the initial pit nucleation step. The onset of pitting in the SNBB-treated steel required a further increase of the anodic potential to +0.50 V_{SCE}, that is, above the corresponding E_{pit} value in this solution.

- Major chromium enrichment in the surface oxide film occurred under anodic polarization conditions both in the presence and the absence of the inhibitor. Angle resolved XPS measurement showed that chromium enrichment progressed into the bulk of the oxide film, and did not occur exclusively at its outermost layer. Because the 304 stainless steel is in the passive state, the concentration of the iron ions released in solution is limited unless sudden dissolution of the passive film due to localized breakdown occurs at sufficiently anodic polarization. That is, significant iron dissolution happened at anodic potentials where the oxy-hydroxide passive layer of stainless steel became unstable in the presence of chloride ions, although pitting nucleation was prevented by the formation of iron-SNBB chelates that precipitate at these sites and block them.

Acknowledgements

M. Talebian expresses his greatest gratitude to Isfahan University of Technology (IUT) for the financial support of a 6-month mobility grant to the University of La Laguna. B.M. Fernández-Pérez and A.M. Betancor-Abreu are grateful to the Canarian Agency for Research, Innovation and Information Society (Las Palmas de Gran Canaria, Spain) and the European Social Fund (Brussels, Belgium) for research contracts. Financial support by the IUT and by the Spanish Ministry of Economy and Competitiveness (MINECO, Madrid) and the European Regional Development Fund, under grant CTQ2016-80522-P, is gratefully acknowledged**.**

References

1. R.L. Plaut, C. Herrera, D.M. Escriba, P.R. Rios, A.F. Padilha, A short review on wrought austenitic stainless steels at high temperatures: Processing, microstructure, properties and performance, Materials Research 10 (2007) 453-460.
2. Outokumpu Stainless AB, Handbook of Stainless Steel, Outokumpu oyj, Espoo, 2013.

3. G.T. Burstein, C. Liu, R.M. Souto, S.P. Vines, Origins of pitting corrosion, Corrosion Engineering Science and Technology 39 (2004) 25-30.
4. P.C. Pistorius, G.T. Burstein, Metastable pitting corrosion of stainless steel and the transition to stability, Philosophical Transactions of the Royal Society London A 341 (1992) 531-559.
5. G.T. Burstein, P.C. Pistorius, S.P. Mattin, The nucleation and growth of corrosion pits on stainless steel, Corrosion Science 35 (1993) 57-62.
6. M.P. Ryan, D.E. Williams, R.J. Chater, B.M. Hutton, D.S. McPhail, Why stainless steel corrodes, Nature 415 (2002) 770-774.
7. J. Jun, K. Holguin, G.S. Frankel, Pitting corrosion of very clean type 304 stainless steel, Corrosion 70 (2013) 146-155.
8. M. Guzmán, R. Lara, Inhibition pitting corrosion of A-890-1B stainless steel in NaCl solution by 5-amino-1,3,4-thiadiazole-2-thiol, International Journal of Electrochemical Science 9 (2014) 3491-3500.
9. J. Jiang, D. Xu, T. Xi, M.B. Shahzad, M.S. Khan, J. Zhao, X. Fan, C. Yang, T. Gu, K. Yang, Effects of aging time on intergranular and pitting corrosion behavior of Cu-bearing 304L stainless steel in comparison with 304L stainless steel, Corrosion Science 113 (2016) 46-56.
10. W. Tian, N. Du, S. Li, S. Chen, Q. Wu, Metastable pitting corrosion of 304 stainless steel in 3.5% NaCl solution, Corrosion Science 85 (2014) 372-379.
11. J. Soltis, Passivity breakdown, pit initiation and propagation of pits in metallic materials – Review, Corrosion Science 90 (2015) 5-22.
12. A.D. Mercer, Corrosion inhibition: Principles and practice, in Corrosion. Volume 2: Metal/Environment Reactions, L.L. Shreir, R.A. Jarman, G.T. Burstein (Editors), 3rd. edition, Butterworth-Heinemann, Oxford, 1994, p. 7:10-7:37.
13. J. Aljourani, K. Raeissi, M. Golozar, Benzimidazole and its derivatives as corrosion inhibitors for mild steel in 1M HCl solution, Corrosion Science 51 (2009) 1836-1843.
14. M.A. Hegazy, A novel Schiff base-based cationic Gemini surfactants: Synthesis and effect on corrosion inhibition of carbon steel in hydrochloric acid solution, Corrosion Science 51 (2009) 2610-2618.
15. M. Finšgar, S. Fassbender, S. Hirth, I. Milošev, Electrochemical and XPS study of polyethyleneimines of different molecular sizes as corrosion inhibitors for AISI 430

stainless steel in near-neutral chloride media, Materials Chemistry and Physics 116 (2009) 198-206.

16. M. Saadawy, The inhibitive effect of a (1,3-dioxolan-2-ylmethyl)–triphenylphosphonium bromide on the corrosion of steel in 0.5 M phosphoric acid, International Journal of Electrochemical Science 8 (2013) 2080-2094.
17. R. Sadeghi Erami, M. Amirnasr, K. Raeissi, M.M. Momeni, S. Meghdadi, Multidentate Schiff bases as new and effective corrosion inhibitors for mild steel in hydrochloric acid solution: an electrochemical and quantum chemical assessment, Journal of the Iranian Chemical Society 12 (2015) 2185-2197.
18. Z. Salarvand, M. Amirnasr, M. Talebian, K. Raeissi, S. Meghdadi, Enhanced corrosion resistance of mild steel in 1 M HCl solution by trace amount of 2-phenyl-benzothiazole derivatives: Experimental, quantum chemical calculations and molecular dynamics (MD) simulation studies, Corrosion Science 114 (2017) 133-145.
19. H. Heydari, M. Talebian, Z. Salarvand, K. Raeissi, M. Bagheri, M.A. Golozar, Comparison of two Schiff bases containing O-methyl and nitro substitutes for corrosion inhibiting of mild steel in 1 M HCl solution, Journal of Molecular Liquids 254 (2018) 177.
20. Z. Wei, P. Somasundaran, P. Duby, Pitting inhibition by surfactants effect of the charge of headgroups, Journal of The Electrochemical Society 151 (2004) B304-B308.
21. Z. Wei, P. Duby, P. Somasundaran, Pitting inhibition of stainless steel by surfactants: an electrochemical and surface chemical approach, Journal of Colloid and Interface Science 259 (2003) 97-102.
22. V.S. Sastri, Green Corrosion Inhibitors: Theory and Practice, John Wiley & Sons, New York, 2012.
23. C. Cardona, A. Torres, J. Miranda-Vidales, J. Pérez, M. González-Chávez, H. Herrera-Hernández, L. Narváez, Assessment of dimethylbenzodiimidazole as corrosion inhibitor of austenitic stainless steel grade 316L in acid medium, International Journal of Electrochemical Science 10 (2015) 1966-1978.
24. H. Leckie, H. Uhlig, Environmental factors affecting the critical potential for pitting in 18–8 stainless steel, Journal of The Electrochemical Society 113 (1966) 1262-1267.
25. H. Man, D. Gabe, The study of pitting potentials for some austenitic stainless steels using a potentiodynamic technique, Corrosion Science 21 (1981) 713-721.

26. R. Loto, Inhibition effect of butan-1-ol on the pitting corrosion of austenitic stainless steel (Type 304), Gazi University Journal of Science 29 (2016) 19-25.
27. G.O. Ilevbare, G.T. Burstein, The role of alloyed molybdenum in the inhibition of pitting corrosion in stainless steels, Corrosion Science 43 (2001) 485-513.
28. G.O. Ilevbare, G.T. Burstein, The inhibition of pitting corrosion of stainless steels by chromate and molybdate ions, Corrosion Science 45 (2003) 1545-1569.
29. N. Soltani, N. Tavakkoli, M. Khayat Kashani, A. Mosavizadeh, E.E. Oguzie, M.R. Jalali, Silybum marianum extract as a natural source inhibitor for 304 stainless steel corrosion in 1.0 M HCl, Journal of Industrial and Engineering Chemistry 20 (2014) 3217-3227.
30. A. Prakash, D. Adhikari, Application of Schiff bases and their metal complexes - A review, International Journal of ChemTech Research 3 (2011) 1891-1896.
31. W. Al Zoubi, Biological activities of Schiff bases and their complexes: a review of recent works, International Journal of Organic Chemistry 3 (2013) 73-95.
32. D. Dey, G. Kaur, A. Ranjani, L. Gayathri, P. Chakraborty, J. ikary, J. Pasan, D. Dhanasekaran, A.R. Choudhury, M.A. Akbarsha, N. Kole, B. Biswas, A trinuclear zinc–schiff base complex: biocatalytic activity and cytotoxicity, European Journal of Inorganic Chemistry 2014 (2014) 3350-3358.
33. M. Talebian, K. Raeissi, M. Atapour, B.M. Fernández-Pérez, Z. Salarvand, S. Meghdadi, M. Amirnasr, R.M. Souto, Inhibitive effect of sodium (E)-4-(4-nitrobenzylideneamino)benzoate on the corrosion of some metals in sodium chloride solution, Applied Surface Science 447 (2018) 852-865.
34. H.M. Irving, H.S. Rossotti, The calculation of formation curves of metal complexes from pH titration curves in mixed solvents, Journal of the Chemical Society (Resumed) (1954) 2904-2910.
35. P. Samide, Adriana, I. Bibicu, Kinetics corrosion process of carbon steel in hydrochloric acid in absence and presence of 2-(cyclohexylaminomercapto) benzothiazole, Surface and Interface Analysis 40 (2008) 944-952.
36. M. Behpour, S.M. Ghoreishi, N. Mohammadi, M. Salavati-Niasari, Investigation of the inhibiting effect of N-[(Z)-1-phenylemethyleidene]-N-{2-[(2-{[(Z)-1phenylmethylidene]amino}phenyl)disulfanyl]phenyl} amine and its derivatives on the corrosion of stainless steel 304 in acid media, Corrosion Science 53 (2011) 3380-3387.

37. S.K. Saha, A. Dutta, P. Ghosh, D. Sukul, P. Banerjee, Adsorption and corrosion inhibition effect of Schiff base molecules on the mild steel surface in 1 M HCl medium: a combined experimental and theoretical approach, Physical Chemistry Chemical Physics 17 (2015) 5679-5690.
38. C.B. Kumar, K.N. Mohana, Corrosion inhibition efficiency and adsorption characteristics of some Schiff bases at mild steel/hydrochloric acid interface, Journal of the *Taiwan Institute* of Chemical Engineers 45 (2014) 1031-1042.
39. S.M. Tawfik, Corrosion inhibition efficiency and adsorption behavior of N, N-dimethyl-4-(((1-methyl-2-phenyl-2, 3-dihydro-1H-pyrazol-4-yl) imino) methyl)-N-alkylbenzenaminium bromide surfactant at carbon steel/hydrochloric acid interface, Journal of Molecular Liquids 207 (2015) 185-194.
40. N.A. Neveen, S. Hassan, E.M. Saad, I.S. Butler, S.I. Mostafa, Preparation, characterization and pH-metric measurements of 4-hydroxysalicylidenechitosan schiff-base complexes of Fe(III), Co(II), Ni(II), Cu(II), Zn(II), Ru(III), Rh(III), Pd(II) and Au(III), Carbohydrate Research 346 (2011) 775-793.
41. A.E.-F. Ouf, M.S. Ali, E.M. Saad, S.I. Mostafa, pH-metric and spectroscopic properties of new 4-hydroxysalicylidene-2-aminopyrimidine Schiff-base transition metal complexes, Journal of Molecular Structure 973 (2010) 69-75.
42. M. Calvin, K.W. Wilson, Stability of chelate compounds, Journal of the American Chemical Society 67 (1945) 2003-2007.
43. M.A. Naghizadeh, D. Nakhaie, M. Zakeri, M.H. Moayed, The effect of dichromate ion on the pitting corrosion of AISI 316 stainless steel Part II: Pit initiation and transition to stability, Corrosion Science 94 (2015) 420-427.
44. R.S. Lillard, Scanning electrode techniques for investigating near-surface solution current densities, in: Analytical Methods in Corrosion Science and Engineering, P. Marcus, F. Mansfeld (Editors), CRC Press, Boca Raton, FL, 2006, p. 571-604.
45. R.M. Souto, B. Normand, H. Takenouti, M. Keddam, Self-healing processes in coil-coated cladding studied by the scanning vibrating electrode, Electrochimica Acta 55 (2010) 4551-4557.

46. M.B. Jensen, D.E. Tallman, Application of SECM to corrosion studies, in Electroanalytical Chemistry: A Series of Advances, Vol. 24, A.J. Bard, C.G. Zoski (Editors), CRC Press, Boca Raton, FL, 2012, p. 171-286.
47. L. Coelho, M. Mouanga, M.-E. Druart, I. Recloux, D. Cossement, M.-G. Olivier, A SVET study of the inhibitive effects of benzotriazole and cerium chloride solely and combined on an aluminium/copper galvanic coupling model, Corrosion Science 110 (2016) 143-156.
48. J. Izquierdo, L. Martín-Ruíz, B.M. Fernández-Pérez, R. Rodríguez-Raposo, J.J. Santana, and R.M. Souto, Scanning microelectrochemical characterization of the effect of polarization on the localized corrosion of 304 stainless steel in chloride solution, Journal of Electroanalytical Chemistry 728 (2014) 148-157.
49. J. Izquierdo, B.M. Fernández-Pérez, L. Martín-Ruíz, V. Mena, R. Rodríguez-Raposo, J.J. Santana, R.M. Souto, Evaluation of the corrosion protection of steel by anodic processing in metasilicate solution using the scanning vibrating electrode technique, Electrochimica Acta 178 (2015) 1-10.
50. G. Williams, A.J. Coleman, H.N. McMurray, Inhibition of aluminium alloy AA2024-T3 pitting corrosion by copper complexing compounds, Electrochimica Acta 55 (2010) 5947-5958.
51. Y. González-García, G.T. Burstein, S. González, R.M. Souto, Imaging metastable pits on austenitic stainless steel in situ at the open-circuit corrosion potential, Electrochemistry Communications 6 (2004) 637-642.
52. H. Hillborg, U.W. Gedde, Hydrophobicity changes in silicone rubbers, IEEE Transactions on Dielectrics and Electrical insulation 6 (1999) 703-717.
53. S. Merzlikin, Depth Profiling by X-ray Photoelectron Spectroscopy, Dissertation, Ruhr-Universität Bochum, Bochum, 2007.
54. V.S. Sastri, Corrosion Inhibitors, Principles and Applications, Wiley, Chichester, 1998.
55. U.R. Evans, CXL.—The passivity of metals. Part I. The isolation of the protective film, Journal of the Chemical Society (Resumed) (1927) 1020-1040.
56. J.G.N. Thomas, The mechanism of corrosion prevention by inhibitors, in: L.L. Shreir, R.A. Jarman, G.T. Burstein (Eds.), Corrosion, Vol. 2, Corrosion Control, 3rd Edn., Butterworth-Heinemann, Oxford, 2000, pp. 17:52-17:65.

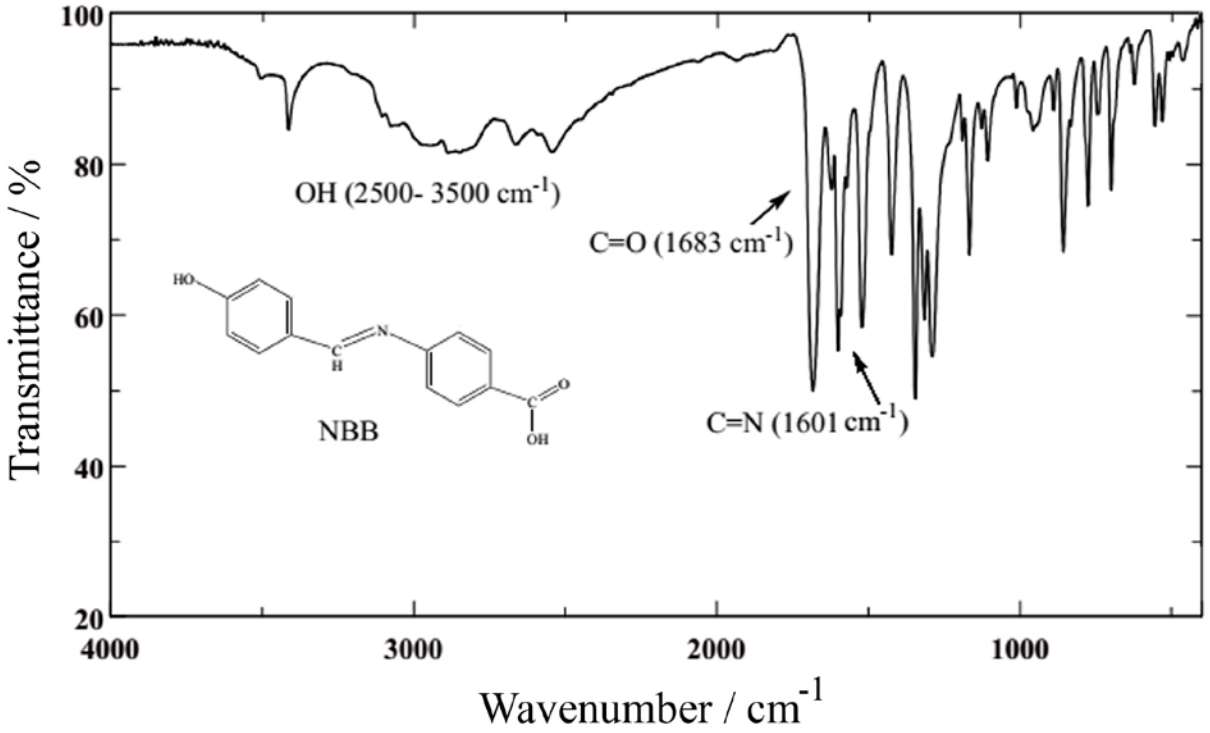

Figure 1. FT-IR spectrum of synthesized of (E)-4-(nitrobenzylidene-amino)-benzoic acid (NBB).

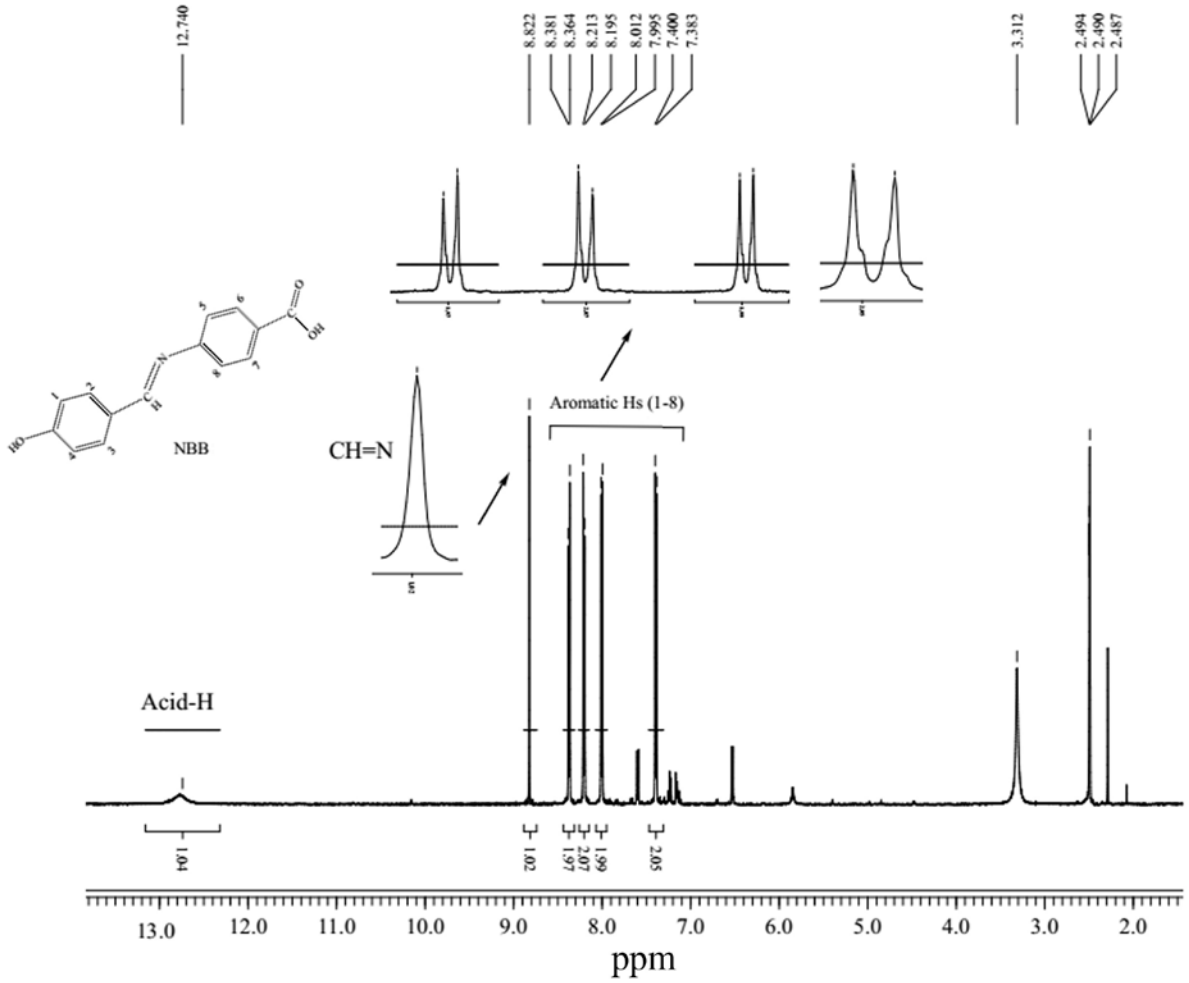

Figure 2. ^{1}H NMR spectrum of synthesized of (E)-4-(nitrobenzylidene-amino)-benzoic acid (NBB).

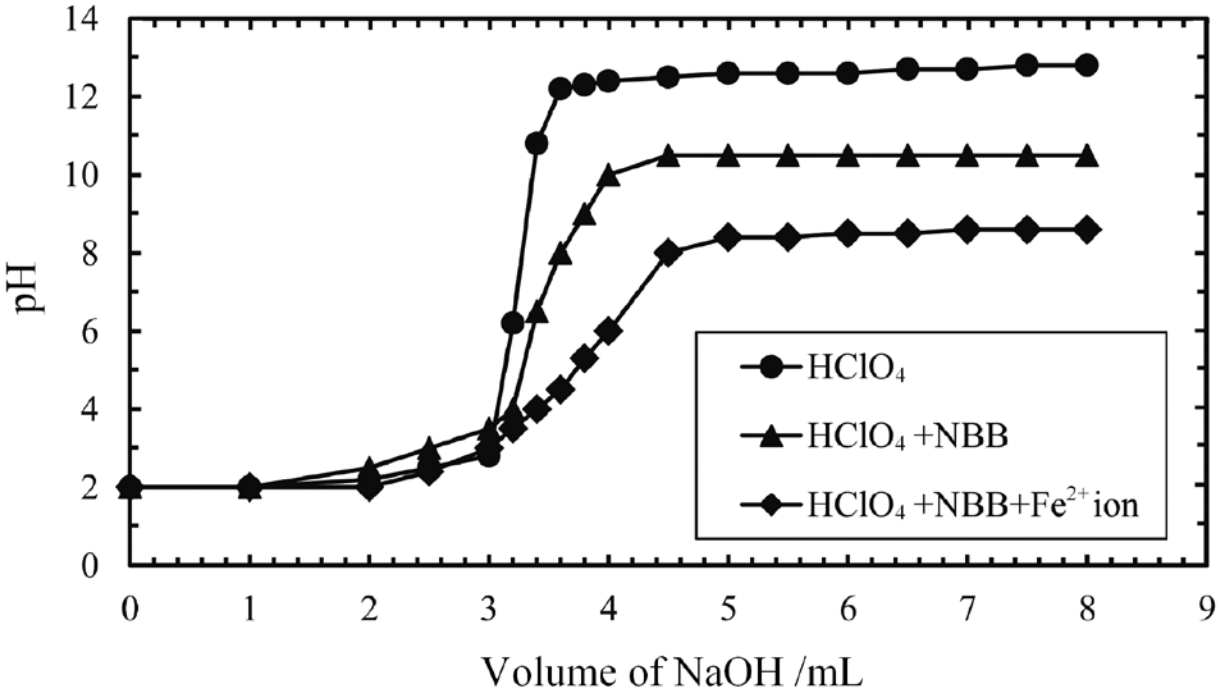

Figure 3. pH titration plots recorded for Solutions 1-3 (ionic strength 1 M) at 25 ºC.

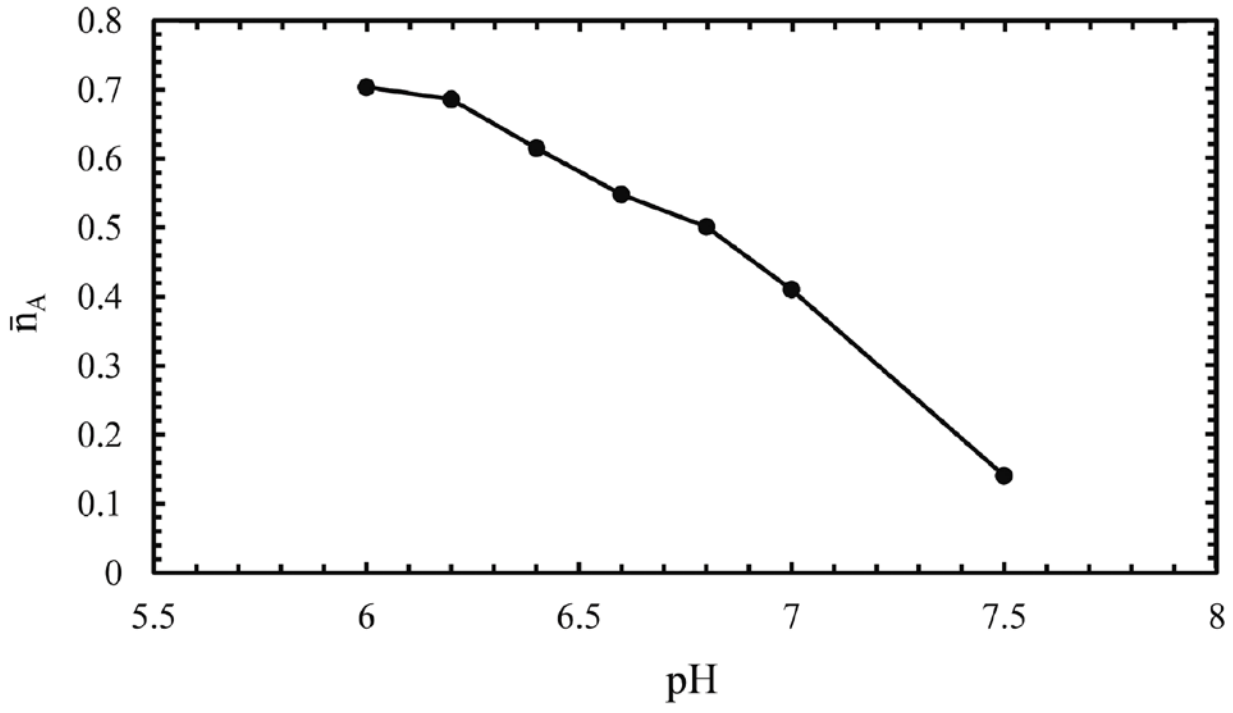

Figure 4. Determination of the deprotonating constant (pK_a) of NBB using the half integral method.

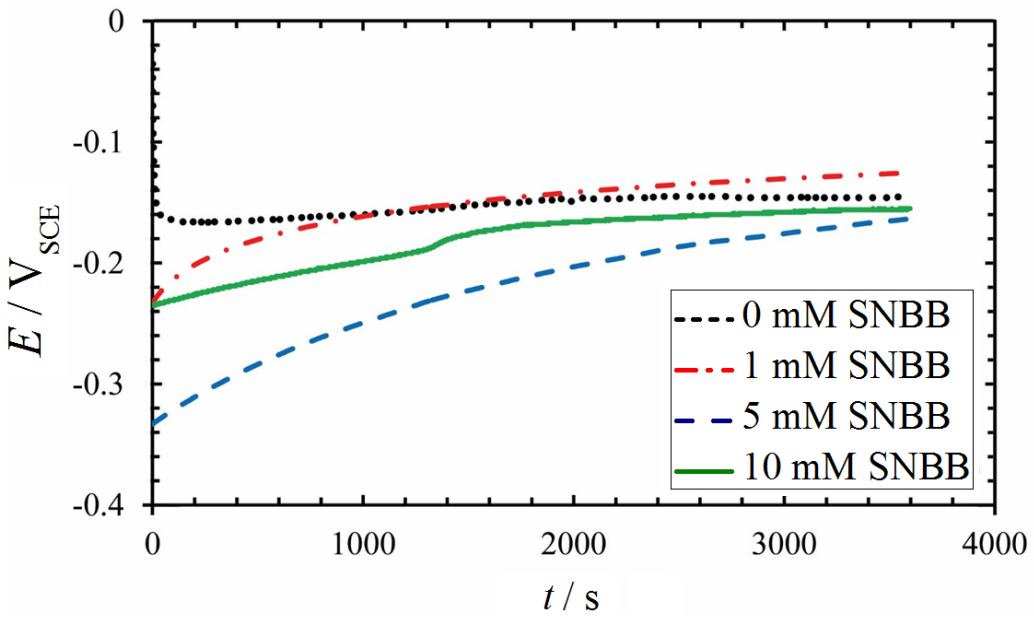

Figure 5. Variation of the open circuit potential (OCP) with time of 304 stainless steel immersed in 0.1 M NaCl solution containing different concentrations of sodium (E)-4-(nitrobenzylidene-amino)-benzoate (SNBB).

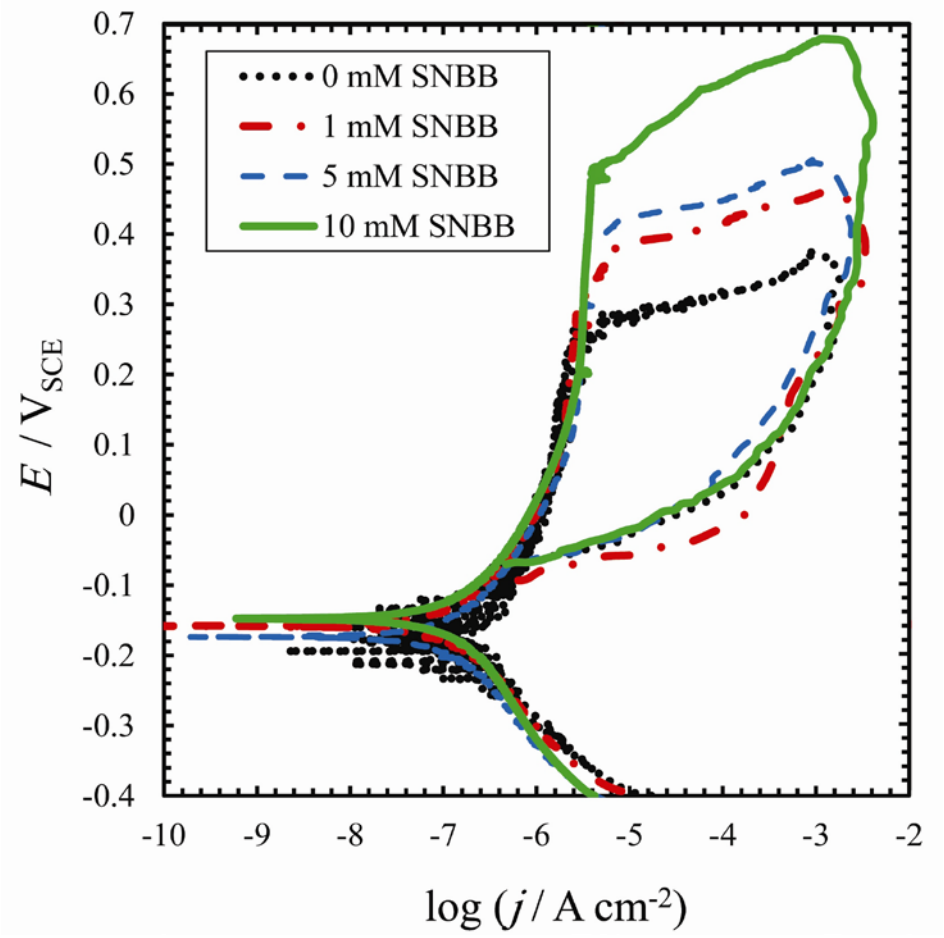

Figure 6. Cyclic potentiodynamic polarization curves of 304 SS immersed in 0.1 M NaCl containing different concentrations of SNBB. Scan rate, 0.5 mV s^{-1}.

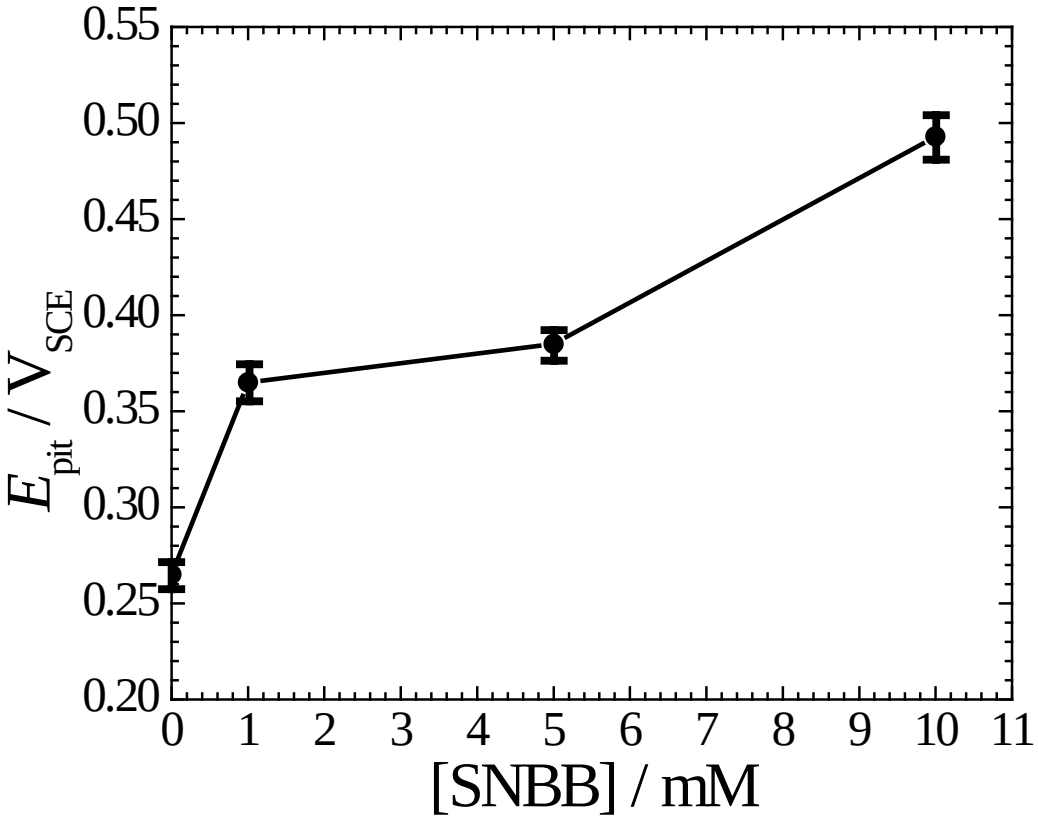

Figure 7. Variation of the pitting potential (E_{pit}) of 304 SS with concentration of SNBB in 0.1 M NaCl solution.

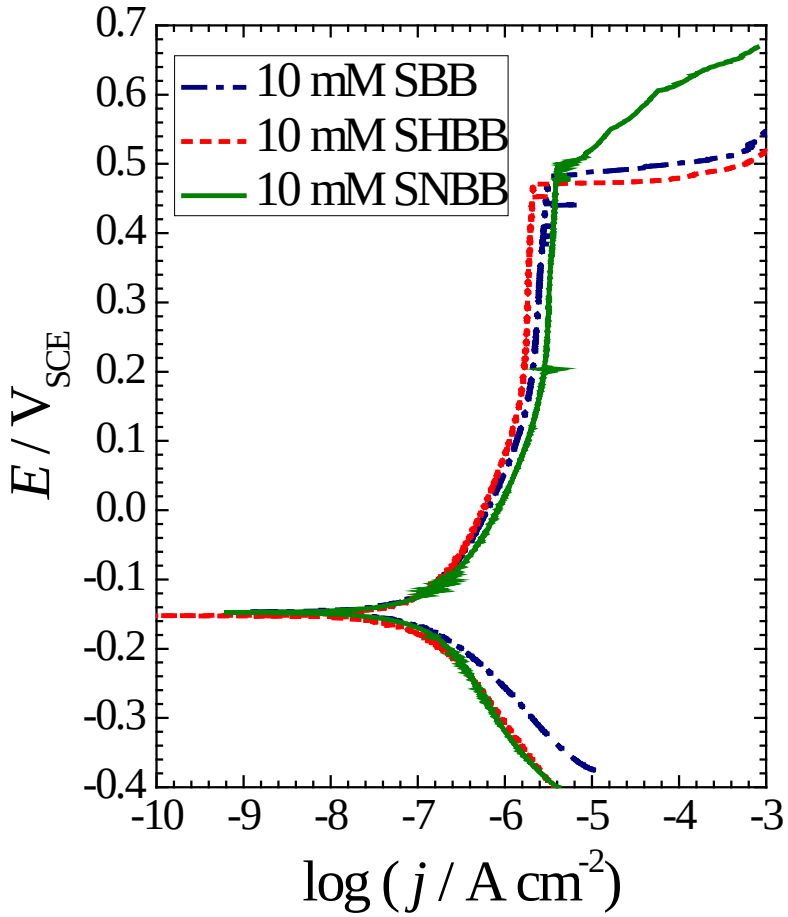

Figure 8. Potentiodynamic polarization curves of 304 SS immersed in 0.1 M NaCl containing 0.01 M of different inhibitors at 25 ºC. Scan rate, 0.5 mV s^{-1}.

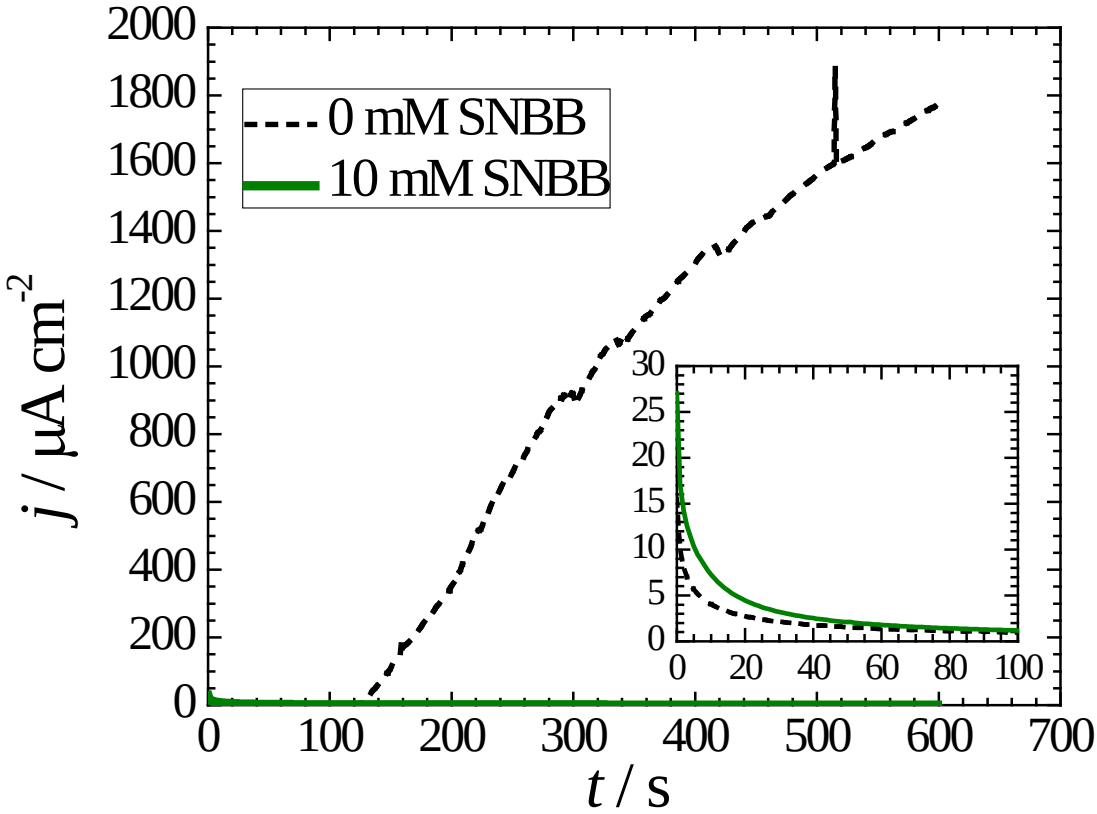

Figure 9. Potentiostatic polarization tests performed at +0.40 V_{SCE} in 0.1 M NaCl + *x* M SNBB (*x* = 0, 0.01) solution at 25 ºC.

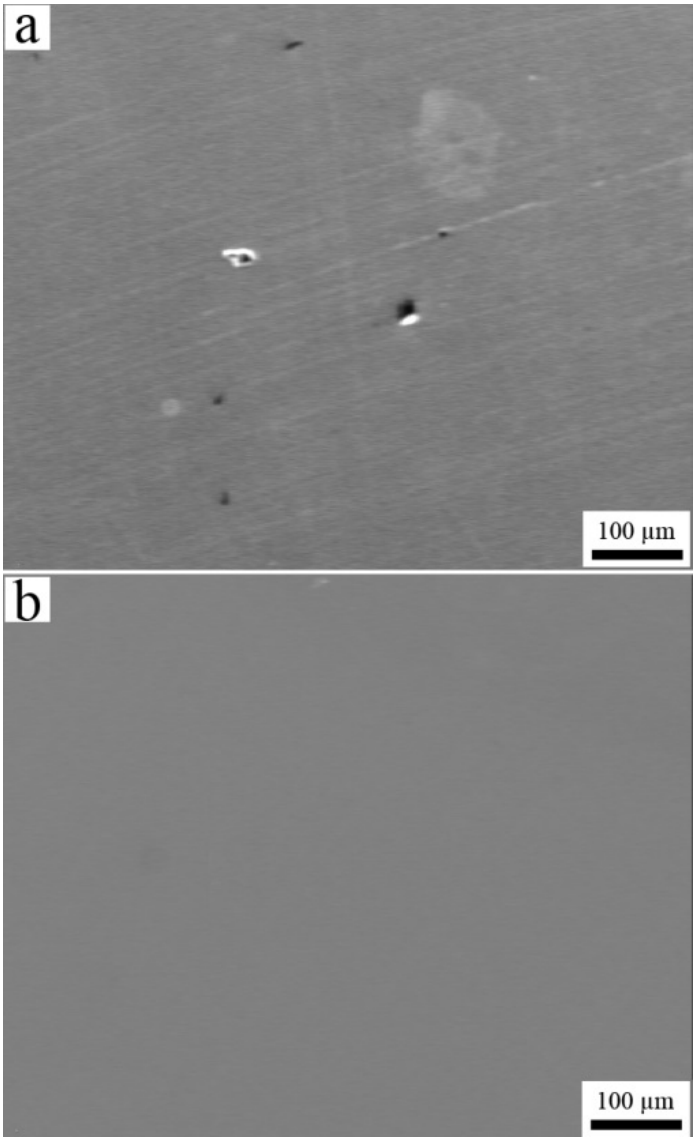

Figure 10. SEM characterization of 304 SS samples retrieved after recording the potentiostatic polarization curves of Figure 9. Test solution: (a) 0.1 M NaCl, and (b) 0.1 M NaCl + 0.01 M SNBB.

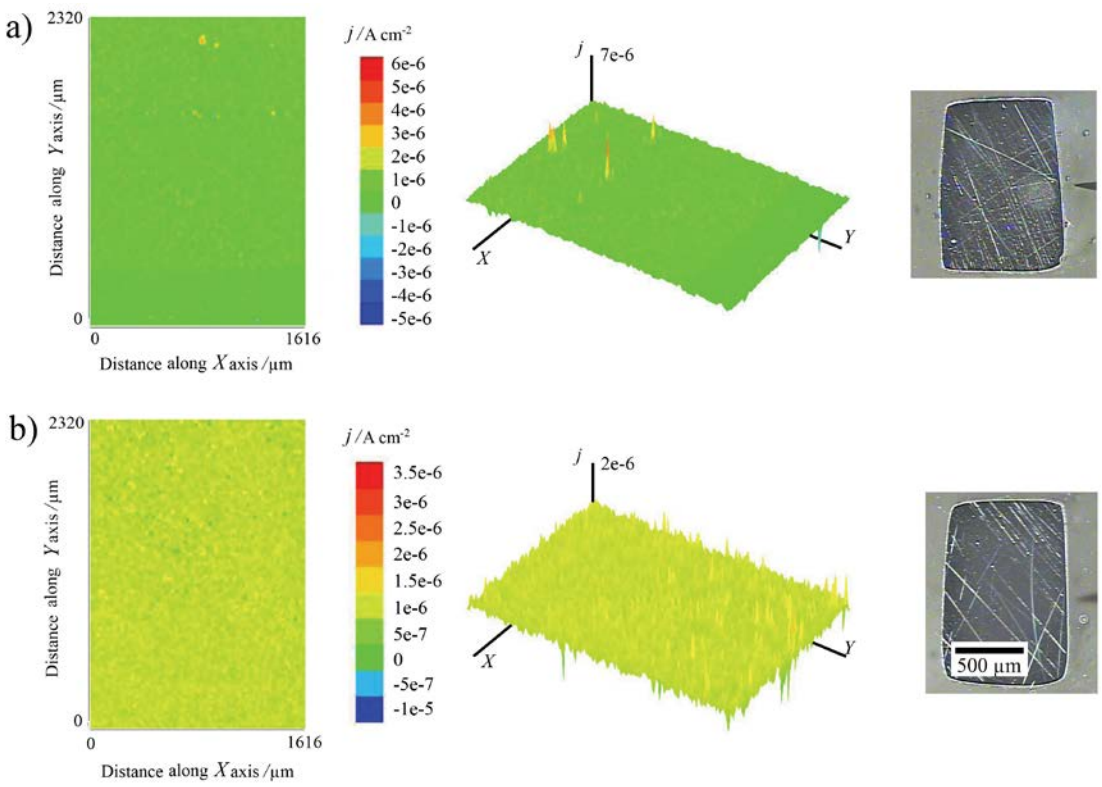

Figure 11. SVET images and optical micrographs of 304 stainless steel strips immersed in (a) 0.1 M NaCl, and (b) 0.1 M NaCl + 10 mM SNBB. The samples were left at their corresponding OCP values in the electrolyte for 60 min before starting to record the SVET images. Tip-substrate distance: 50 µm.

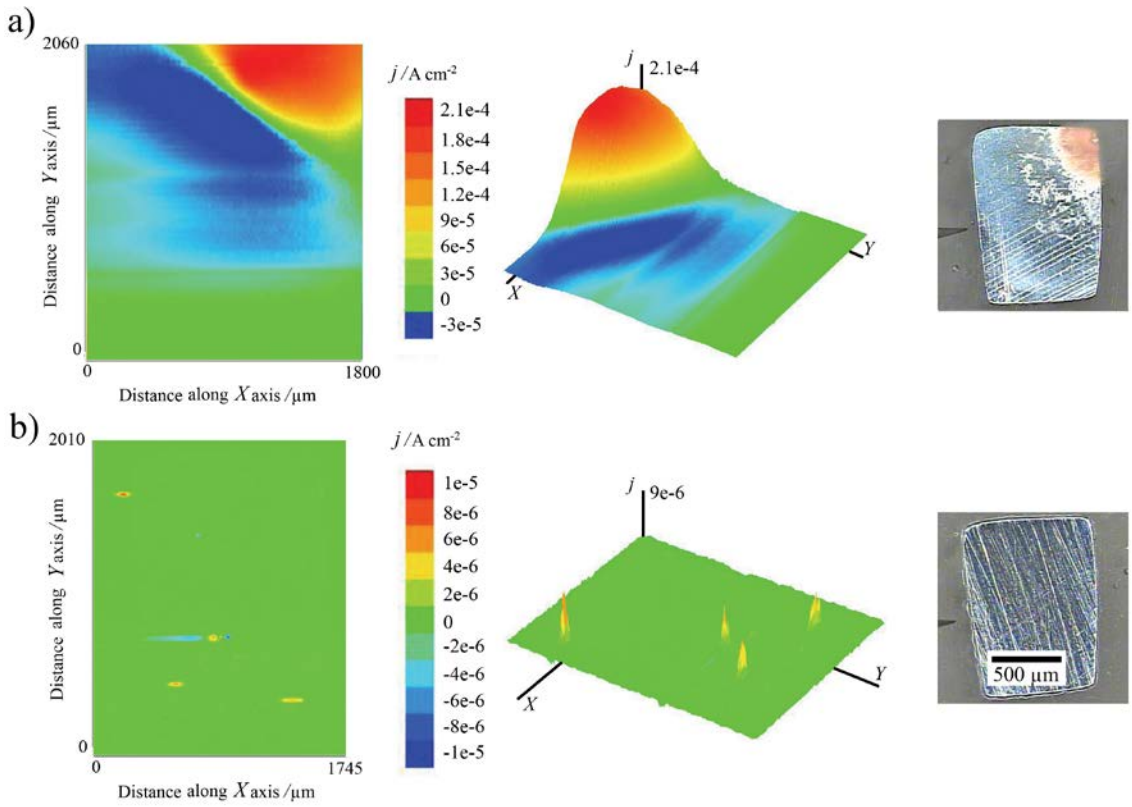

Figure 12. SVET images and optical micrographs of 304 stainless steel strips immersed in (a) 0.1 M NaCl, and (b) 0.1 M NaCl + 10 mM SNBB while anodically polarized at +0.40 V_{SCE}. Prior to imaging, the samples were left at their corresponding OCP values in the electrolyte for 60 min. Tip-substrate distance: 50 µm.

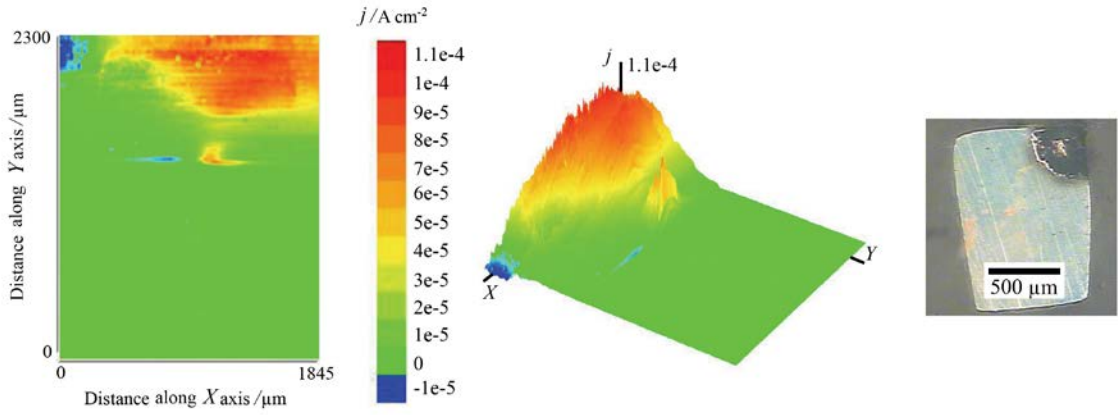

Figure 13. SVET images and optical micrograph of a 304 stainless steel strip immersed in (b) 0.1 M NaCl + 10 mM SNBB while anodically polarized at +0.50 V_{SCE}. Prior to imaging, the sample was left at its corresponding OCP value in the test electrolyte for 60 min. Tip-substrate distance: 50 μm.

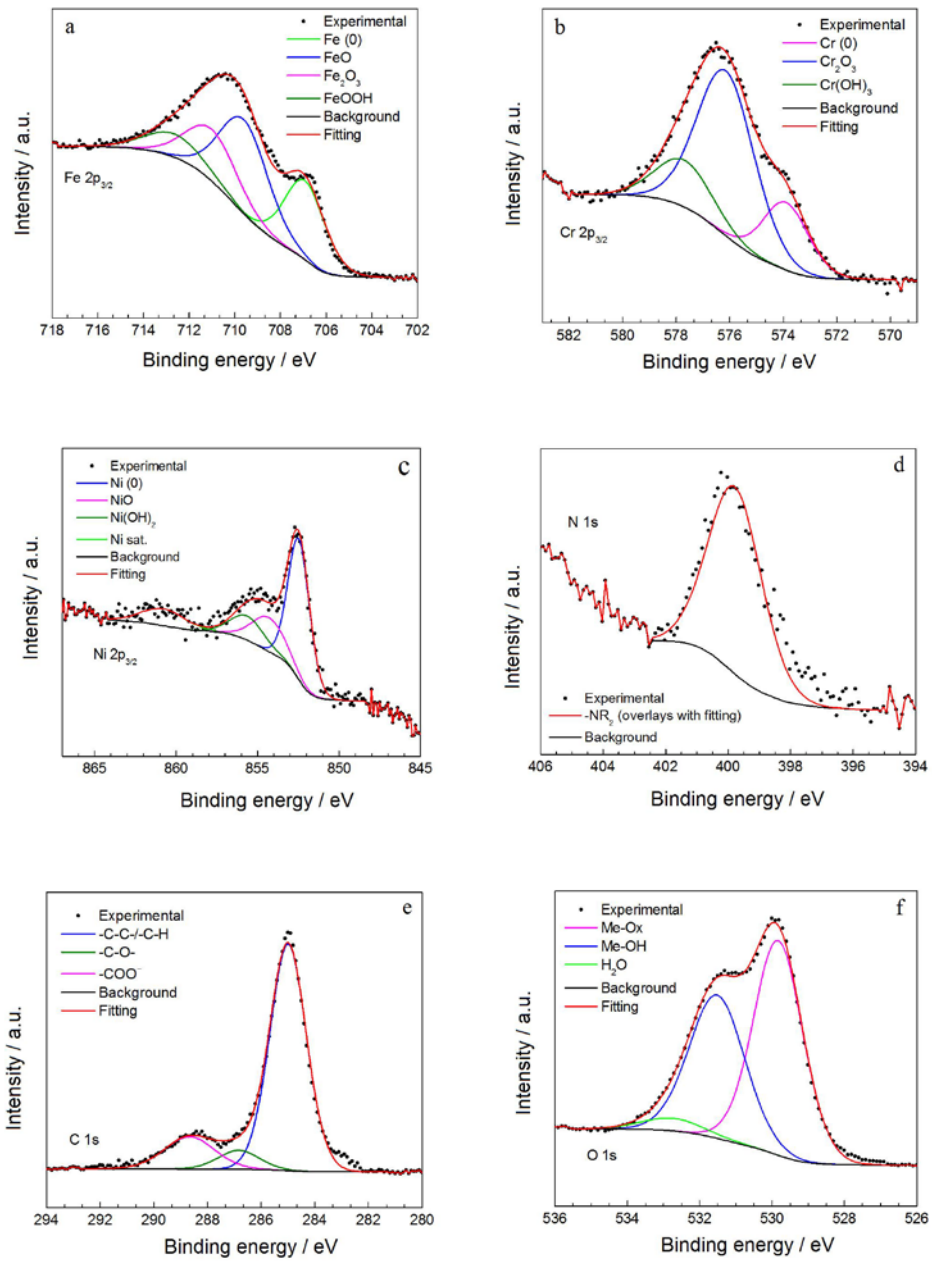

Figure 14. Deconvoluted Fe $2p_{3/2}$, Cr $2p_{3/2}$, Ni $2p_{3/2}$, N 1s, C 1s, and O 1s XPS spectra of 304 stainless steel after 1 h immersion in 0.1 M NaCl solution followed by potentiostatic polarization at +0.45 V_{SCE} for 600 s (sample code IV). All high-resolution spectra shown were recorded at a emission angle of 5 degrees on sample II, with the exception of N 1s that was recorded at the same emission angle but on sample IV (i.e., the only sample that showed an unambiguous signal for N 1s).

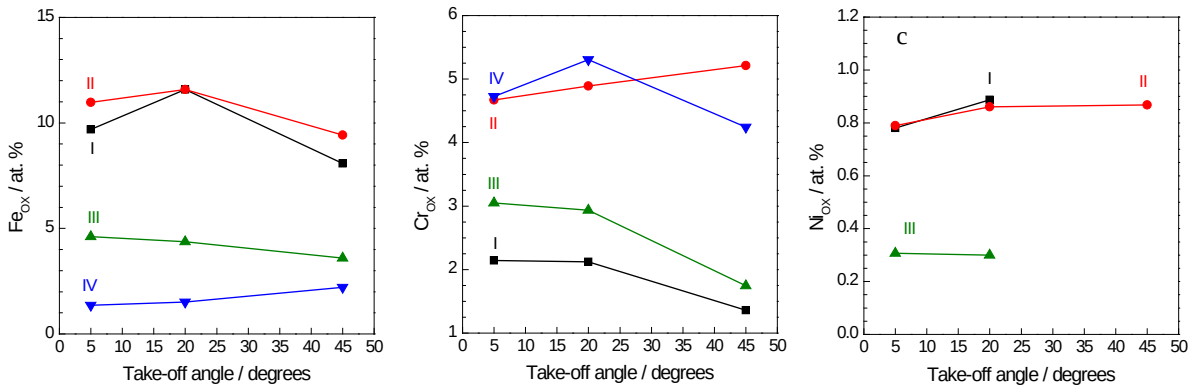

Figure 15. Variation of the oxide component (in at.%) for (a) Fe, (b) Cr, and (c) Ni, with the emission angle of XPS spectra for samples indicated in Table 4. The percentages are the contribution of the oxide species to the total amount of each element.

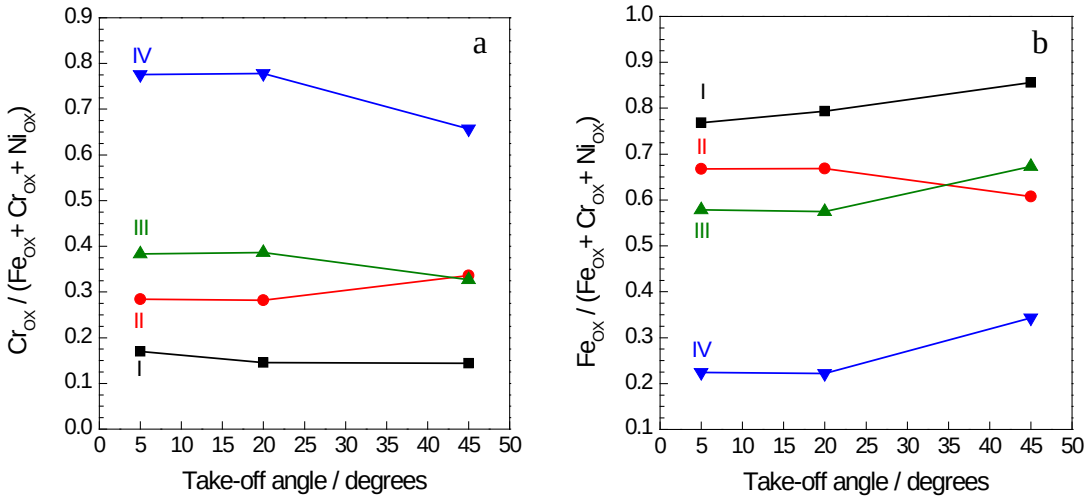

Figure 16. Variation of the oxide layer composition, expressed as the cationic fractions of (a) Cr and (b) Fe, with the emission angle of XPS spectra for samples indicated in Table 4.

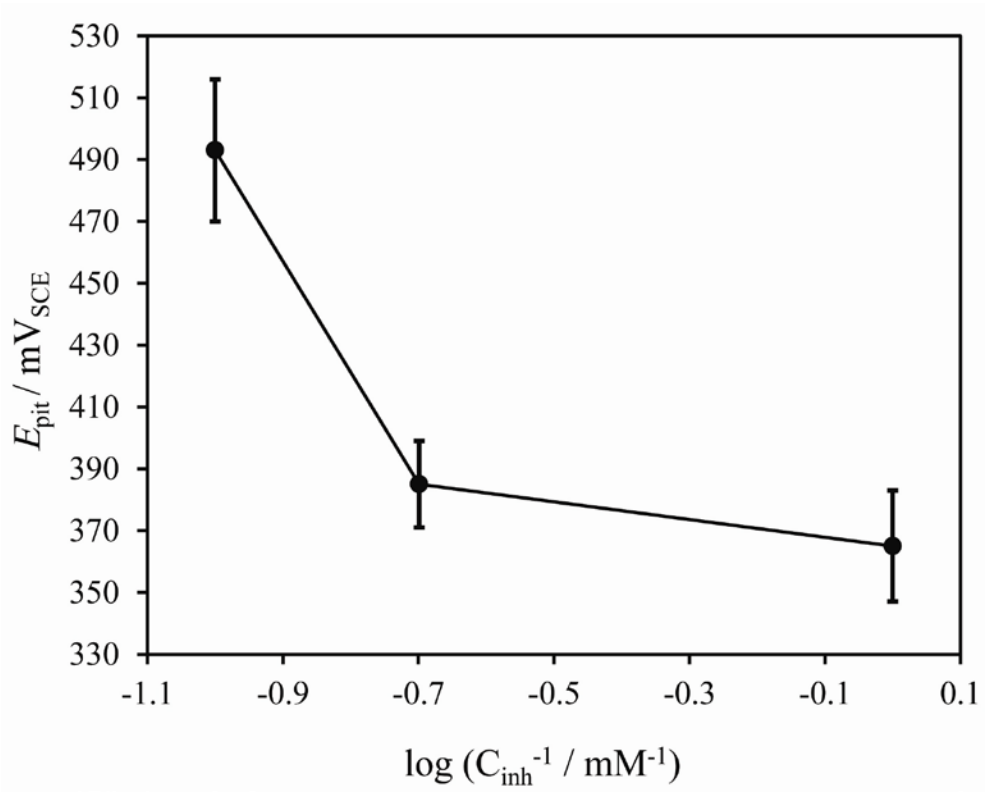

Figure 17. Relationship between E_{pit} and log(C_{inh}^{-1}) for 304 stainless steel immersed in 0.1 M NaCl + 10 mM SNBB solution.

Table 1. Chemical composition of synthesized of (E)-4-(nitrobenzylidene-amino)-benzoic acid (NBB)

	Element / wt.%		
	C	H	N
Calculated	62.22	3.73	10.37
Observed	62.55	3.87	10.20

Table 2. IUPAC names, structures, and molecular weights of the three synthesized inhibitors.

IUPAC name	Structure	Abbreviation	Molecular weight / g mol^{-1}
Sodium (E)-4-(nitrobenzylidene-amino)-benzoate	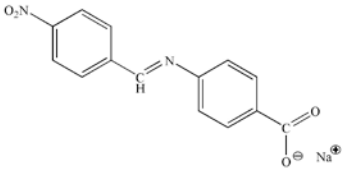	SNBB	292.22
Sodium (E)-4-(benzylidene-amino)-benzoate	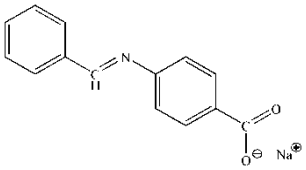	SBB	247.22
Sodium (E)-4-(hydroxybenzylidene-amino)-benzoate	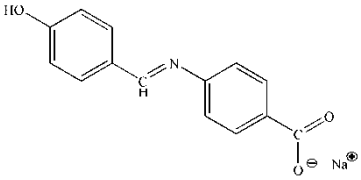	SHBB	263.22

Table 3. Electrochemical parameters obtained from the potentiodynamic polarization results of 304 SS immersed in 0.1 M NaCl containing different concentrations of the synthesized inhibitors at 25 ºC.

Inhibitor	c_{inh} / mM	E_{corr} / mV_{SCE}	j_{corr} / μA cm^{-2}	E_{pit} / mV_{SCE}	E_{rp} / mV_{SCE}	j_{pass} / μA cm^{-2}	Width of the passive region / mV
--	0	-171 ± 13	0.25 ± 0.01	265 ± 15	-70 ± 10	2.24 ± 0.02	436 ± 20
SNBB	1	-156 ± 18	0.13 ± 0.01	365 ± 18	-62 ± 12	2.48 ± 0.01	521 ± 25
SNBB	5	-173 ± 11	0.12 ± 0.02	385 ± 14	-97 ± 08	3.09 ± 0.01	558 ± 18
SNBB	10	-146 ± 11	0.10 ± 0.01	493 ± 23	-70 ± 12	3.24 ± 0.01	639 ± 25
SHBB	10	-144 ± 19	0.13 ± 0.02	480 ± 21	-68 ± 11	2.91 ± 0.01	624 ± 28
SBB	10	-146 ± 13	0.14 ± 0.01	469 ± 32	-81 ± 15	2.24 ± 0.02	615 ± 35

Table 4. Surface conditioning of the 304 SS samples characterized by XPS.

Sample codes	Treatment procedure
I	Without treatment
II	1 h immersion in 0.1 M NaCl
III	1 h immersion in 0.1 M NaCl + 10 mM SNBB
IV	1 h immersion in 0.1 M NaCl + 10 mM SNBB, followed by potentiostatic polarisation at E = +0.45 V_{SCE} during 600 s in the same solution